Probing the Electrode–Electrolyte Interface of a Model K-Ion Battery Electrode The Origin of Rate Capability Discrepancy between Aqueous and Non-Aqueous Electrolytes

Pierre Lemaire, Alessandra Serva, Mathieu Salanne, Gwënaelle Rousse, Hubert Perrot, Ozlem Sel, Jean-Marie Tarascon

Probing the Electrode-Electrolyte Interface of a Model K-ion Battery Electrode – the Origin of Rate Capability Discrepancy Between Aqueous and Non-Aqueous Electrolytes

Pierre Lemaire[†,‡,§], Alessandra Serva[□], Mathieu Salanne[□,□], Gwënaelle Rousse,[†,‡,§,□], Hubert Perrot[¦], Ozlem Sel[†,§,*] and Jean-Marie Tarascon[†,§,*]

[†] Chimie du Solide et de l'Energie, UMR 8260, Collège de France, 11 Place Marcelin Berthelot, 75231 Paris Cedex 05, France

[‡] Sorbonne Université, 4 Place Jussieu, 75005 Paris, France

[§] Réseau sur le Stockage Electrochimique de l'Energie (RS2E), CNRS FR 3459, 33 Rue Saint Leu, 80039 Amiens Cedex, France

[□] Sorbonne Université, CNRS, Physico-chimie des Électrolytes et Nanosystèmes Interfaciaux, PHENIX, F-75005 Paris

[□] Institut Universitaire de France (IUF), 75231 Paris Cedex 05, France

[¦] Sorbonne Université, CNRS, Laboratoire Interfaces et Systèmes Electrochimiques, LISE, UMR 8235, 4 Place Jussieu, 75005 Paris, France

KEYWORDS: K-ion battery, interface characterization, EQCM, non-aqueous electrolyte, aqueous electrolyte, molecular dynamics

ABSTRACT: Li-ion batteries are the electrochemical energy storage technology of choice of today's electrical vehicles and grid applications with a growing interest for Na-ion and K-ion systems based on either aqueous or non-aqueous electrolyte for power, cost and sustainable reasons. The rate capability of alkali metal-ion batteries is influenced by ions transport properties in the bulk of the electrolyte, as well as by diverse effects occurring at the vicinity of the electrode and electrolyte interface. Therefore, identification of the predominant factor affecting the rate capability of electrodes still remains a challenge and requires suitable experimental as well as computational methods. Herein we investigate the mechanistic of the K^+ insertion process in the Prussian blue phase, $Fe_4{}^{III}[Fe^{II}(CN)_6]_3$ in both aqueous and non-aqueous electrolytes which reveals drastic differences. Through combined electrochemical characterizations, electrochemical-quartz-crystal-microbalance and *ac*-electrogravimetric analyses, we provide evidences that what matters the most for fast ion transport is the positioning of the partially solvated cations adsorbed at the material surface in aqueous as opposed to non-aqueous electrolyte. We rationalized such finding by molecular dynamics simulations that establish the K^+ repartition profile within the electrochemical double layer. A similar trend was early reported by our group for the aqueous *vs.* non-aqueous insertion of Li^+ into $LiFePO_4$. Such a study unveils the critical but overlooked role of the electrode-electrolyte interface in ruling ion transport and insertion process. Tailoring this interface structuring *via* the proper salt-solvent interaction is the key to enabling the best power performances in alkali metal-ion batteries.

1. INTRODUCTION

Our society will increasingly need clean energy. Thus, battery energy storage to facilitate the development of electric transportation and the wide use of renewable intermittent energies will become more important than ever in the past. Autonomy, lifetime, safety, cost, and sustainability are the overriding figure of merits to be put forward in today's battery development roadmaps. However, the power performance, *i.e.* rate capability, often discarded, is also a variable to take into account in the improvement process to implement the battery usage in the full spectrum of energy-related devices. The rate capability of alkali metal-ion batteries is intuitively correlated to the ions' transport properties in the bulk of the

electrolyte, *e.g.* ionic conductivity and transference number, which has been a pivotal point for the development of current electrolyte formulations and their further improvement regarding the charge carrier's transport through understanding the ion-ion and ion-solvent interactions.[1-4] The enhanced ionic transport properties when moving from lithium to potassium ions is rationalized by the weaker Lewis acidity of the latter.[5] This results in a smaller Stockes radius, *i.e.,* cation and its solvation shell, and therefore an easier vehicle-type displacement in the bulk of the electrolyte when a concentration gradient is imposed. Another parameter, not to be disregarded, is the desolvation energy of the cation in the bulk of the electrolyte, which is modified when moving from Li^+ to Cs^+ within the alkali metal column. Regardless of the nature of the electrolyte (non-aqueous or aqueous), the desolvation energy decreases when moving from lithium to potassium ion. Worth noting also is that the dehydration energy is yet always higher than desolvation energy in an organic electrolyte.[5, 6] To examine the factors that may affect the rate performance, it is convenient to split the insertion mechanism into several steps, in which the solvated cation diffuses from the bulk of the electrolyte to the electrode interface, then it desolvates, is inserted in the host material and subsequently diffuses in the bulk of the material. The insertion mechanism can alter depending on the surface chemistry of the electrode[7] and by the evolution of the surface, such as solid electrolyte interface (SEI) or cathode electrolyte interface (CEI) formation.[8, 9] In the latter cases, the role of ion transfer across solution/ SEI (or CEI) and across SEI (or CEI)/electrode interface on the rate capability should also be taken into account.[8] Therefore, it is evident that determining the predominant factor affecting the rate capability of electrodes is a complex issue and requires careful consideration of several aspects with suitable experimental as well as computational methods.

Our group previously evidenced that the insertion process in Li-ion host material (shown for $LiFePO_4$ (LFP)) is assisted by solvent molecules at the electrode-electrolyte interface (EEI).[10] In addition, this solvent-assisted mechanism seems to govern the rate capability difference found between the organic and aqueous electrolytes. This can be explained by a higher desolvation energy of Li ions at the organic than at the aqueous electrolyte interface, in contrast with the expectations based on the bulk properties.[10] To strengthen the robustness of the results obtained with the Li-ion host, LFP, concerning the solvent-assisted insertion mechanism and the prominence of the solvation shell on the rate capability, we decided to explore other alkali metal-ion batteries. Potassium ions that feature a smaller and weaker solvation shell in the bulk of the electrolyte appear as the ideal candidates to untangle the different steps taking place during the cation insertion and to confirm the significance of the desolvation step. Thus, a K-ion host, Prussian Blue (PB, $KFe^{III}[Fe^{II}(CN)_6]$) has been selected herein as a model compound. Potassium ions can be inserted in the PB phase either in aqueous[11-13] and non-aqueous electrolytes.[14] Another benefit of PB is that it can be electrodeposited, enabling an easy thickness and morphology control of the deposits. It can be noted that $FePO_4$ is also known as K-ion host; however, K^+ can only be inserted in the amorphous and porous phase, which is incompatible with purely gravimetric measurements.[15]

To convey our results, we will first report the electrodeposition of the PB thin films that thickness-homogeneity and surface roughness are conform for an *operando* EQCM study, prior to present the electrochemical-gravimetric analyses performed to demonstrate the prominence of the ions' desolvation step on the battery kinetics. Then, combined experimental (EIS and EQCM coupling, also called *ac*-electrogravimetry) and computational methods (classical molecular dynamics simulations at fixed potential) are presented to identify the species involved in the interfacial processes and the structure of the electrochemical double layer, respectively, prior to propose a clear picture of the dynamic electrode-electrolyte interface during the insertion process. Altogether, we unambiguously demonstrate that K^+ insertion in Prussian Blue phase follows the same rate capability discrepancy between aqueous and non-aqueous electrolytes, alike what we had previously reported for the aqueous or non-aqueous Li^+ insertion in $LiFePO_4$.[10]

2. MATERIALS AND METHODS

2.1. Prussian Blue thin film electrode preparation: The PB phase was prepared by electrodeposition at the surface of a gold disk electrode or directly on one side of the gold patterned quartz resonator (8.95 MHz ± 50 kHz, QA-A9M-AU(M)). The EQCM electrode was protected in a dedicated mask exposing only the gold surface area of 0.196 cm^2. The phase was deposited from a solution containing 0.01 $mol.L^{-1}$ HCl (37 %, Carlo Erba), 0.02 $mol.L^{-1}$ $K_3[Fe(CN)_6]$ (> 99 %, Sigma-Aldrich) and 0.02 $mol.L^{-1}$ $FeCl_3$ (> 98%, Alfa Aesar). The solutions were prepared separately at higher concentration to be diluted to the desired concentration and mixed in the mentioned order prior usage. A 3 mm diameter graphite rod (Sigma-Aldrich) and Hg/Hg_2SO_4 (saturated K_2SO_4) protected with a frit containing a solution of K_2SO_4 0.25 $mol.L^{-1}$ (99 %, Alfa Aesar) were used as the counter and the reference electrode, respectively. The solution was stirred during electrodeposition time. A -40 $\mu A.cm^{-2}$ cathodic current (-7.84 µA for

a surface area of 0.196 cm^2) was applied during different period of time: 150, 300, 450 and 600 s, to obtain different thicknesses of PB film: 100, 200, 300 and 400 nm, respectively (see Supporting Information, part 3-5). The PB phase is formed following this redox Equation 1:

$$3\,Fe(CN)_6^{3-} + 4\,Fe^{3+} + 3\,e^- \rightleftarrows Fe_4^{III}[Fe^{II}(CN)_6]_3 \qquad \text{Equation 1}$$

A 1 µm thick film was prepared at the surface of a gold disk electrode to check the structural phase by X-ray diffraction. Then, the films were cycled 15 times in aqueous medium containing 0.25 $mol.L^{-1}$ K_2SO_4 at pH 3.5 to insert potassium ion in the structure which was described in the literature to result in the removal of one ferric iron,[16, 17] as shown in the Equation 2:

$$Fe_4^{III}[Fe^{II}(CN)_6]_3 + 3\,K^+ \rightleftarrows 3\,KFe^{III}[Fe^{II}(CN)_6] + Fe^{3+} \qquad \text{Equation 2}$$

After this step, the films can be cycled in the same aqueous electrolyte or in a non-aqueous electrolyte (0.5 $mol.L^{-1}$ KPF_6 in 50:50 ethylene carbonate (EC) and diethyl carbonate (DEC)). For the latter, the films were dried under vacuum overnight at 80 °C.

2.2. Materials characterization: X-ray diffraction (XRD) was performed to confirm the success of the synthesis using a BRUKER D8 Advance diffractometer with Cu Kα radiation ($\lambda_{K\alpha1}$ = 1.54056 Å, $\lambda_{K\alpha2}$ = 1.54439 Å). Rietveld refinement,[18] was performed to obtain structural parameters as implemented in the FullProf suite.[19] The crystal structures shown in this work were drawn with the VESTA visualization program,[20] using the crystallographic information obtained from Rietveld refinements. Additionally, the morphology of the electrodeposited films was observed by Scanning Electron Microscopy (SEM) with a SU-70 Hitachi FEG-SEM (accelerating voltage of 5 keV). The sample was covered with a thin layer of gold (10 nm) using a plasma sputtering coater (MTI, GSL-1100X-SPC-12).

2.3. Electrochemical characterization:

2.3.1. Electrochemical-gravimetric measurements: The specifically designed EQCM cell was kept at 25 °C during the experiment thanks to a temperature-controlled oven. A commercial SEIKO QCM922A microbalance was connected to the cell through a BNC cable to monitor the resonance frequency change (Δf) along with the motional resistance (R) during the electrochemical processes. The microbalance was coupled with a SP-200 potentiostat (Bio-Logic SAS), which permitted the recording of microbalance outputs and the realization of simultaneous electrochemical measurements. Prior to the measurement, the EQCM was calibrated to determine the experimental sensitivity coefficient (*i.e.* proportionality constant between the change of quartz frequency and change of mass) in the Sauerbrey equation.[21] Here, an experimental sensitivity coefficient of 1.21 ± 0.03 ng Hz^{-1} was used, the details were previously given.[10]

The electrodes were cycled in the desired electrolyte: KPF_6 0.5 $mol.L^{-1}$ in EC:DEC 1:1 for the organic electrolyte or K_2SO_4 0.25 $mol.L^{-1}$ (pH 3.5) for the aqueous analogue. For aqueous electrolyte, a 3 mm diameter graphite rod (Sigma-Aldrich) and Hg/Hg_2SO_4 (saturated K_2SO_4) were used as the counter and the reference electrodes, respectively. For organic electrolyte, potassium metal (99.9 %, Sigma-Aldrich) of 2 mm were punched to be used as both counter and reference electrodes. All the cell parts were dried overnight at 80 °C before being assembled in an Ar-filled glovebox (MBraun, O_2 and H_2O < 0.1 ppm), before each experiment using non-aqueous electrolytes.

2.3.2. Ac-electrogravimetry: Ac-electrogravimetric measurements were carried out by using a four-channel frequency response analyzer (Solartron 1254 FRA) and a laboratory-made potentiostat and QCM. The QCM was used under dynamic regime, working electrode (PB coated EQCM electrode mentioned in *Section 2.3.1*) was polarized at a selected potential, and a small-amplitude potential perturbation (40 mV rms) was superimposed. The frequency range was between 63 kHz and 10 mHz for the potential modulation. The details of the measurement were given elsewhere.[11, 22, 23] Further details and theoretical background are given in Supporting Information, part 8.

2.4. Classical Molecular Dynamics simulations: Classical MD simulations of 0.25 $mol.L^{-1}$ K_2SO_4 in H_2O and 0.5 $mol.L^{-1}$ KPF_6 in 50:50 ethylene carbonate (EC) and diethyl carbonate (DEC) between two planar Au(100) electrodes at a fixed potential difference of 0 V were performed with the MetalWalls code.[24] Each electrode is made of 5 layers, 162 Au atoms each, while the electrolyte is composed of 25 K_2SO_4 ion pairs and 5500 H_2O molecules for the aqueous system and of 50 KPF_6 ion pairs and 558 EC / 558 DEC molecules for the non-aqueous system.

The SPC/E[25] model was chosen for water, while force field parameters for EC and DEC were taken from OPLS[26] with charges adopted in Chaudhari *et al.*[27] In the aqueous system, the Lennard-Jones parameters for K^+ and force field parameters for SO_4^{2-} were taken from Yu *et al.*[28] and Pegado *et al.*[29] respectively, with charges scaled by 0.94. In the non-aqueous systems, the Lennard-Jones parameters for K^+ were taken from OPLS,[26] while force field parameters for PF_6^- from Canongia Lopes *et al.*[30] Finally, Lennard-Jones parameters introduced by Heinz *et al.*[31] were adopted for Au(100). Mixed Lennard–Jones parameters for all of

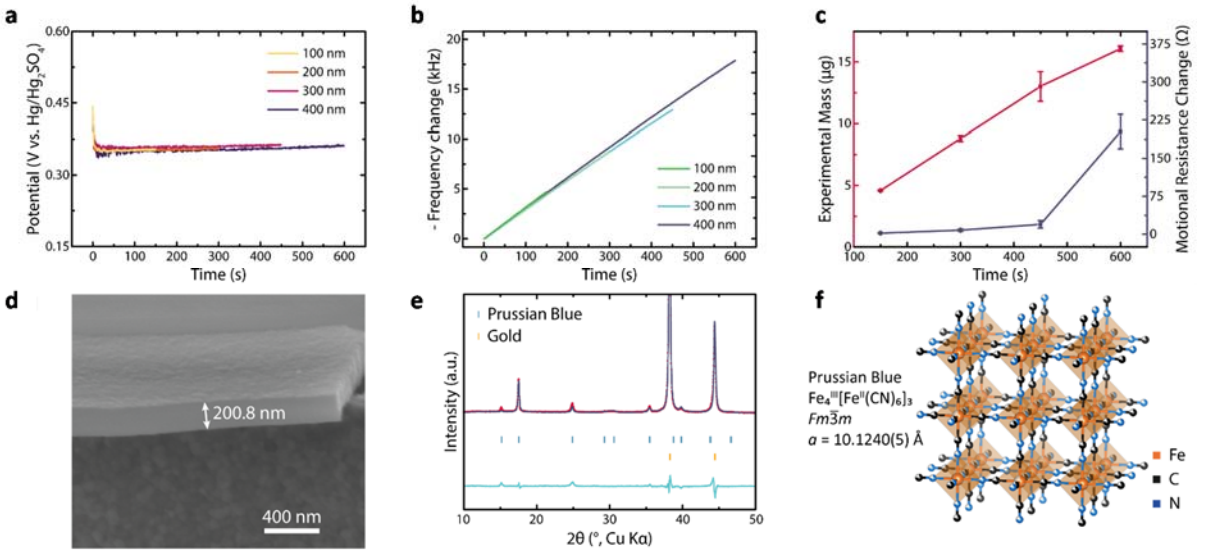

Figure 1. (a) Electrodeposition of PB *via* chronopotentiometry at -40 µA.cm^{-2} in HCl 0.01 mol.L^{-1}, $K_3[Fe(CN)_6]$ 0.02 mol.L^{-1} and $FeCl_3$ 0.02 mol.L^{-1}, (b) *operando* frequency measurement by EQCM during different periods of time, (c) experimental mass and motional resistance for PB films measured in air, (d) Thickness estimation of the electrodeposited film by FEG-SEM through a cross section sample, (e) Rietveld refinement of XRD patterns of a 1 µm thick PB film on a gold substrate (The red circles, dark blue continuous line and bottom blue line represent the observed, calculated and difference patterns, respectively. PB phase and gold are indexed by blue and orange bars, respectively. Refinement parameters are: R_p=12.9%; R_{wp}=15.5% and the χ^2=6.14) and (f) the corresponding structural model, including $[Fe(CN)_6]$ vacancies.

the different atom types were obtained using the Lorentz–Berthelot combination rules.

2D periodic boundary conditions were employed, with no periodicity on the direction normal to the Au surface and box dimensions along x and y directions of Lx = Ly = 36.63 Å. Electrostatic interactions were computed using a 2D Ewald summation method, with a cut-off of 12 Å for the short-range part. The simulation boxes were equilibrated at constant atmospheric pressure by applying a constant pressure force to the electrodes. The electrodes separation was then fixed to the equilibrium value. An equilibration run of 2 ns in the NVT ensemble (T = 298K) was then performed. After equilibration, production runs of 40 ns have been collected in the NVT ensemble (T = 298K), with the electrodes potential fixed to 0 V. Note that this corresponds to point of zero charge (PZC) conditions, but previous simulations works have shown that for such concentrated electrolytes the structure of the double-layer (characterized by the distance of the ions to the electrodes and their solvation shell at the interface) is not affected much in the range of experimentally accessible potentials.[24] The Gaussian charge distribution width of the gold atoms was fixed to a value of 0.40 Å to mimic the low metallic character[32] of the Prussian blue electrode used in the experiments. The time step was set to 1 fs for K_2SO_4 in H_2O and 2 fs for KPF_6 in EC:DEC.

3. RESULTS AND DISCUSSION

3.1. Phase preparation and characterization: The PB phase was prepared by electrodeposition at the surface of gold patterned quartz resonators in an acidic solution containing ferric and ferricyanide ions. A constant -40 µA.cm^{-2} cathodic current was applied during different periods of time (t_{ED}): 150, 300, 450 and 600 s, to obtain theoretical thicknesses of 100, 200, 300 and 400 nm, respectively. The electrochemical curves for electrodeposition procedure are plotted in Figure 1a. They show a plateau of potential, which is independent of the deposition time, characteristic of the $Fe_4{}^{III}[Fe^{II}(CN)_6]_3$ electrodeposition (Prussian Blue) following Equation 1. The resonant frequency of the quartz resonator was monitored during the electrodeposition process and the opposite of the frequency change (directly proportional to the mass change) is represented in Figure 1b. The mass linearly increases and its slope is practically independent of the electrodeposition time, indicating the formation of films with different thickness but rather similar molar mass. As evidenced by their low motional resistance change with respect to their loadings, the films with nominal thicknesses ≤ 300 nm are suitable for electrogravimetric studies as given in Figure 1c (details can be found in the Supplementary Information, part 3).

The FEG-SEM images of the films (shown only for the 100 nm film thickness in Figure 1d) indicate that the electrodeposited films are conformal and sufficiently flat at the surface of the quartz resonator, independently of the film thickness. In addition to the resonators used as substrates for EQCM studies, a relatively thick film (1 µm, t_{ED} of 1500 s) of PB was also prepared on a gold disk electrode. X-ray diffraction was used to characterize the electrodeposited phase, the XRD pattern is presented in Figure 1e. It shows both intense peaks characteristic of the gold substrate and relatively less intense peaks, which can be indexed in a cubic $Fm\bar{3}m$ unit cell, in agreement with the reported $Fe_4^{III}[Fe^{II}(CN)_6]_3$ PB phase. Figure 1f depicts the structural model deduced from the Rietveld refinement, which shows a cubic structure with a lattice parameter of 10.1240(5) Å.

3.2. Electrochemical and electrogravimetric analyses:

3.2.1. Rate capability assessment: After the 15 cycles of pre-treatment, the potassium ions are inserted in the PB structure, as shown in Equation 3:

$$KFe^{III}[Fe^{II}(CN)_6] + K^+ + e^- \rightleftarrows K_2Fe^{II}[Fe^{II}(CN)_6] \quad \text{Equation 3}$$

The rate capability assessment is performed on PB films of different thickness, which were cycled in an aqueous electrolyte composed of K_2SO_4 0.25 mol.L^{-1} (pH 3.5) and in non-aqueous electrolyte composed of KPF_6 0.5 mol.L^{-1} in EC:DEC 1:1. The K^+ concentration was kept constant at 0.5 mol.L^{-1} between the two media, for the sake of comparison. Here K_2SO_4 salt was preferred over KCl to avoid the Cl^- insertion into the PB structure[16, 33] and above mentioned organic electrolyte is the most frequently used by the battery community according to Hwang *et al.*[34] The film was solely reversibly cycled between Prussian Blue

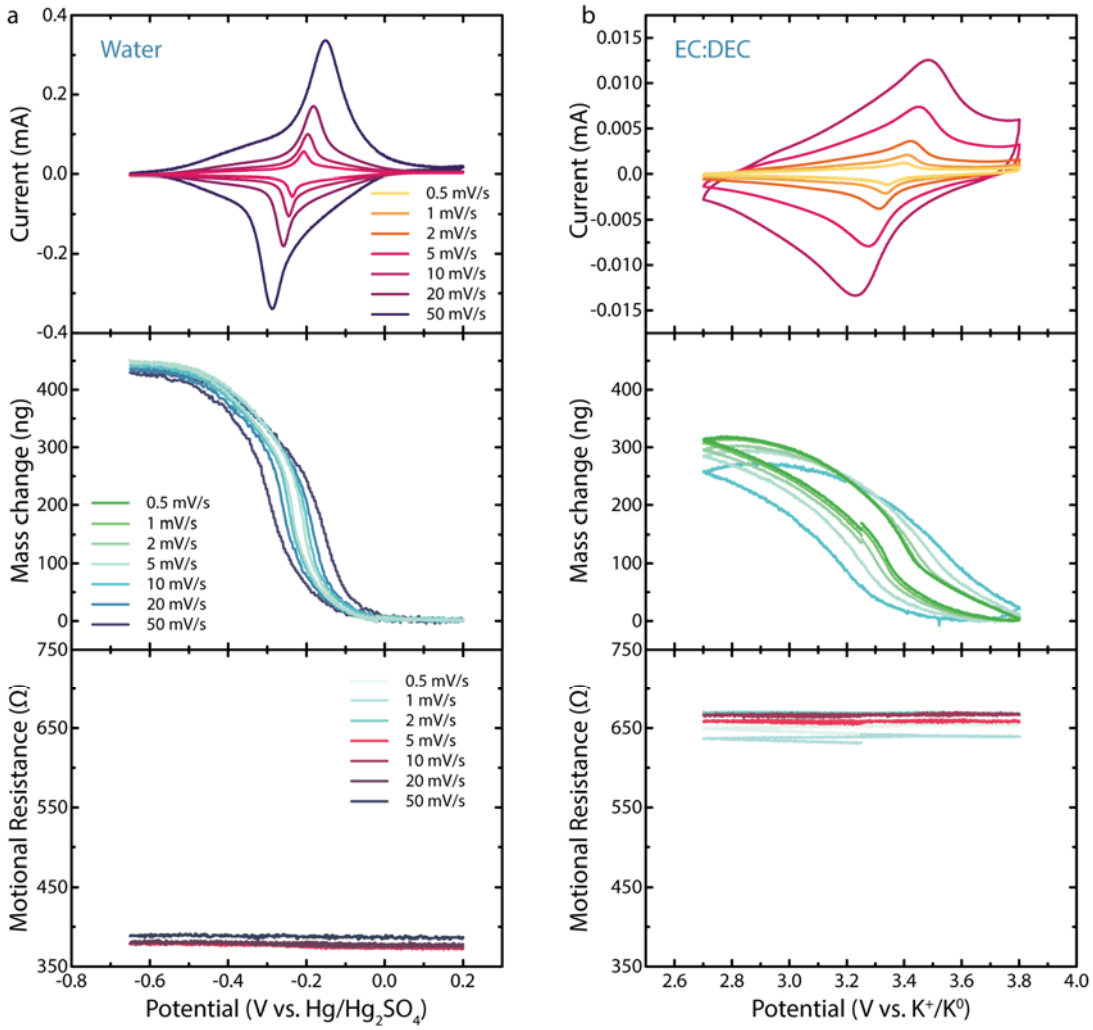

Figure 2. Cyclic voltammetry of a 100 nm thick PB film at different scan rates, in (a) 0.25 mol.L^{-1} K_2SO_4 in H_2O (pH 3.5) and (b) 0.5 mol.L^{-1} KPF_6 in EC:DEC. Current (top), mass changes (middle) and absolute motional resistance (bottom) were simultaneously measured. The frequency change was converted into mass change, using Sauerbrey equation. The fifth cycle is here represented for each scan rate.

($KFe^{III}[Fe^{II}(CN)_6]$) and Prussian White ($K_2Fe^{II}[Fe^{II}(CN)_6]$) (Equation 3), without reaching the Prussian Green phase ($Fe^{III}[Fe^{III}(CN)_6]$). Frequency change (translated into mass change) and absolute motional resistance were simultaneously monitored during cyclic voltammetry (CV) at various scan rates. The results obtained for each electrolyte and at each scan rate are gathered in the Figure 2.

Although all films have been cycled, results are solely reported for the 100 nm thick film as no difference was detected as a function of the thickness. The motional resistance, R (Figure 2, bottom panel) drastically increases from aqueous to non-aqueous electrolyte, which is easily explainable by the Kanazawa and Gordon equation,[35] and is related to the increase of liquid viscosity and density (from H_2O to EC:DEC). In addition, R shows no variation in both electrolytes during CV regardless of the scan rates. The steadiness of the motional resistance monitoring proves the rigidity retention,[36] during the potassium insertion/extraction and therefore the purely gravimetric regime (see Supporting Information file, part 3). It is noted that for the present binder-free inorganic coatings, EQCM-R is perfectly suitable to evaluate the gravimetric regime. These results were also in good agreement with the electroacoustic measurements.[37]

Classical electrochemical response (Figure 2, top panel) of PB was observed in both aqueous and organic electrolytes. Aqueous electrolyte presents sharper peaks than organic electrolyte even if the CV has been performed at faster scan rates. Moreover, the non-aqueous electrolyte shows a larger hysteresis between the oxidation and reduction peaks. Altogether, these features evidence the lower rate capability of the PB phase in non-aqueous electrolyte. To quantify the difference in the rate capability, the charge passing through the system during reduction was measured for the various scan rate in both electrolytes (Figure S5). The PB films with a thickness of ~100 nm leads to a specific discharge capacity of 85.9 mAh.g^{-1} obtained in aqueous electrolytes, which nearly equals the theoretical capacity of $KFe^{III}[Fe^{II}(CN)_6]$ (87.33 mAh.g^{-1}). In non-aqueous electrolytes, discharge capacity values approaching to that in the aqueous electrolyte is nearly obtained, but at very low cycling rate. The reason why the curves were found to cross at very low rate and diverge at high rate is typical of kinetic limitations (Figure S5). The similarity of the results previously obtained with the LFP phase[10] proves that changing the alkali metal ion does not affect the rate capability trend found between aqueous and non-aqueous electrolytes. The mass response of the electrodes (Figure 2, middle) also reveals the difference of rate capability. A more pronounced

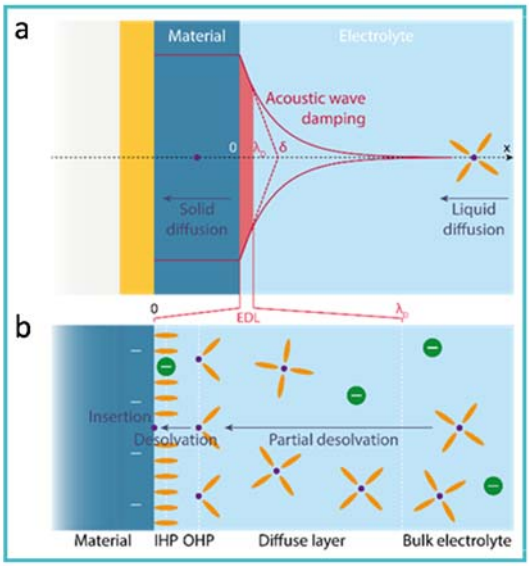

Figure 3. Schematic representation of the insertion of an alkali metal cation in a host material. (a) Comparison between the penetration depth of acoustic wave from the QCM to the solution (δ) and the electrochemical double layer characteristic length (λ_D). (b) Close-up snapshot of the electrochemical double layer during cation insertion.

hysteresis is observed in organic electrolyte and it is confirmed further in the spreading of the mass change over a larger potential window. Lastly, when the scan rate increases, almost no difference is visible in the total mass variation in water-based electrolyte, which is the opposite behavior in the organic counterpart, further stressing the rate capability difference between both electrolytes.

3.2.2. Determination of the rate-limiting step: The CV and EQCM-R analyses in the previous section clearly demonstrated a difference in rate capability due to a change in the electrolyte solvent (H_2O to EC:DEC), but a remaining question regards the origin of such a difference. The insertion mechanism can be broken down into various steps: *i.* diffusion of the solvated cation from the bulk of the electrolyte to the electrode interface, *ii.* desolvation of the cation (termed as specific adsorption of a solvated cation which occurs through a charge transfer between the electrode and the adsorbed ion[38]), *iii.* insertion of the bare cation in the host material related to the charge transfer and *iv.* diffusion of the cation in the bulk of the material.[39] These different steps are sketched in Figure 3. In addition to these steps, the surface layer formation, such as SEI or CEI can modify the ion insertion mechanism and in this case the ion transfer across solution/ SEI (or CEI) and across SEI (or CEI)/electrode interface should also be considered among the predominant steps.[8] To explain the difference of kinetics, the rate-limiting

step needs to be identified, bearing in mind all the processes mentioned above.

First of all, ions' transport properties in the bulk of the electrolyte is investigated,[2] to see if this difference of behavior can be explained by the dissimilarity in liquid ionic conductivity of the two types of electrolytes. The ionic conductivities were experimentally measured for both aqueous and non-aqueous electrolytes and are equal to 42.8 $mS.cm^{-1}$ and 6.39 $mS.cm^{-1}$, respectively. A significant dissimilarity is found; however, using the Nernst-Einstein equation, the liquid ionic diffusion coefficient of potassium ion is estimated and turns out to be in the same order of magnitude of 10^{-5} $cm^2.s^{-1}$ for both electrolytes. This diffusion coefficient is much higher than that in the bulk of the material. Moreover, it should be counterbalanced by the use of slower scan rates in the organic electrolyte; such an effect is not observed in neither the CV nor the EQCM results. These points make the liquid diffusion unlikely to be the rate-limiting step.

As a next step, the transport properties inside the electrode were investigated. To this end, the K^+ diffusion coefficient in PB was scrutinized by two different electrochemical techniques. Firstly, Potentiostatic Intermittent Titration Technique (PITT) was used at different potentials during potassium insertion and extraction in both electrolytes, according to the protocol developed in the Supplementary Information, part 1 and Figure S1. PITT analysis was applied to the PB films with different thicknesses; the results are gathered in Figure S2. The first prominent result is the good agreement between the diffusion coefficient estimated during ion insertion and extraction, regardless of the film thickness and the electrolyte. Moreover, the solid diffusion coefficient is logically independent of the film thickness. Finally, the absolute value of the diffusion coefficient is also equivalent (≈ 10^{-12} $cm^2.s^{-1}$) in water-based and EC:DEC-based electrolytes. As expected, the solid diffusion coefficient of potassium ion is several orders of magnitude smaller than the liquid ionic diffusion coefficient.

For the sake of comparison, the solid diffusion coefficient of potassium ion was also estimated by using the Randles-Sevcik equation and the CV responses performed earlier for rate capability assessment (Figure 2, upper panels). The Figure 4c gathers the results obtained for insertion and extraction peaks, for the different film thicknesses in the two electrolytes.

As for the PITT results, no difference is detected between insertion and extraction process in both electrolytes (Figure 4c). However, a massive dissimilarity is present between aqueous and non-aqueous electrolytes, when the solid diffusion coefficient is estimated by the Randles-Sevcik equation (Figure 4c). Two orders of magnitude separate the two electrolytes. Comparing the results obtained by the Randles-Sevcik equation with the previous PITT results (for the 200 nm thick film in Figure 4), a good agreement exists between the results obtained in water-based electrolyte by the Randles-Sevcik equation and those obtained by PITT measurements in both electrolytes. This equality further demonstrates that the solid diffusion is not the rate-limiting step. As compared to PITT that is performed at equilibrium, the Randles-Sevcik is a dynamic technique by nature. The latter also captures transport phenomenon occurring at the interface. It is therefore likely that the interfacial properties are the key to explain the difference between the

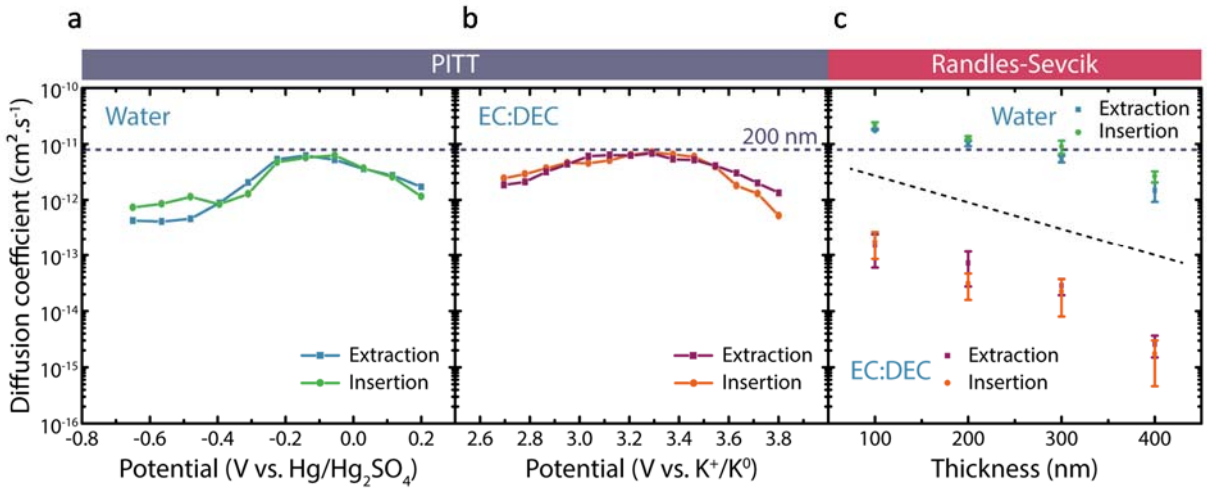

Figure 4. Comparison of the solid diffusion coefficient of potassium ion in PB films of 200 nm, obtained (a, b) by PITT and (c) by the Randles-Sevcik equation. For the PITT results obtained at different film thicknesses refer to Figure S2.

two types of electrolytes. Regarding the two remaining steps, *i.e.* desolvation and charge transfer (in the absence of any alteration of the structure of the film/electrolyte interface due to a SEI or CEI layer formation), it can be supposed that the charge transfer only depends on the material, which has been kept constant during this study. The absence of a surface layer formation has been verified by EQCM-R results and discussed in 3.2.3. Then, the desolvation taking place at the particular EEI can be hypothesized as the prominent step, affecting the battery performance by impeding the insertion kinetics.

3.2.3. First evidence of the potassium solvation shell at the interface: The desolvation process taking place at the interface can be probed by *operando* EQCM analyses. Figure 5 shows the comparison between the electrochemical mass variation associated to the potassium insertion/extraction processed from the charge passing through the system (thanks to the Faraday's law) and the mass variation estimated by the Sauerbrey equation for both electrolytes using the EQCM data presented in Figure 2. The trends are totally different when electrolytes are compared. A drastic difference in mass variation can be observed in the case of the aqueous electrolyte, whereas, in the organic counterpart, these values fit smoothly. As mentioned in Section 3.2.2, CEI formation can modify the ion insertion mechanism. It is noted that there is no noticeable irreversible mass which would correspond to a CEI layer formation,[8] in the organic electrolyte within the voltage window of the study (Figure 5b). Additionally, the R_m values during the measurements shown in Figure 2b and 5b remain unchanged, CEI formation would increase this value (acting as a perturbation for the acoustic wave which finds more difficulties in crossing the passivating layer). Therefore, it is not taken into account among the possible reasons behind the rate limitations difference observed here, between aqueous and organic electrolytes. This more complex response observed for the aqueous case is a first hint towards the participation of water molecules into the insertion mechanism, as this result demonstrates the involvement of a species with a molar mass higher than K^+. Such a mass difference corresponds to a nearly 100 Hz difference between theoretical and experimental frequency changes, leading to around 0.61 water molecule per K^+. The mass per electron, $F\Delta m/\Delta Q$ value, $\left(\frac{M}{z} = F\frac{\Delta m}{\Delta Q} = -FC_f\frac{\Delta f}{\Delta Q}\right)$ was also calculated and represented in the Figure S6 for both electrolytes. These values corroborate the previous findings (Figure 5). In the aqueous electrolyte, the $F\Delta m/\Delta Q$ shows V-shaped curves with a minimum around the insertion/extraction redox potential of potassium insertion into the PB phase at a higher molar mass than K^+, while in the organic counterpart, this value remains steady on a larger potential window, with an absolute value very close to that of the bare K^+. It can be noted that the lower values on the extremities of the potential window may indicate the presence of H_3O^+ or H^+ into the charge compensation process, as already reported.[11, 40]

As schematically pictured in Figure 3a, the desolvation process occurs in the particular electrochemical double layer (EDL) region, which is at the close vicinity of the polarized material. To demonstrate the participation of this process in the QCM measurements, the hydrodynamic layer formed at the surface of the vibrating resonator needs to be compared with the typical width of the double layer. The penetration depth, δ, (transverse acoustic wave propagates for a short distance from the crystal surface to the liquid layer) is the characteristic dimension of the moving liquid layer, as represented in Figure 3a. The δ values are here equal to 189 and 225 nm in water and EC:DEC, respectively (with ρ_l = 1145 kg.m^{-3} and η_l = 1.64 10^{-3} Pa.s for the EC:DEC mixture, according to Wang *et al*[41]) (for 9 MHz resonators used in this study). The characteristic dimension of the EDL is the Debye length, λ_D, which can be obtained thanks to the following Equation 4:

$$\lambda_D = \sqrt{\frac{\varepsilon_0 \varepsilon_R k_B T}{2.10^3 N_A e^2 I}} \qquad \text{Equation 4}$$

where ε_0 is the vacuum permittivity (8.84 10^{-12} F.m^{-1}), ε_R is the relative permittivity (80.1 for water and 40.6 for the EC:DEC mixture[42]), k_B is the Boltzmann constant (1.38 10^{-23} J.K^{-1}), T is the temperature (K), N_A is the Avogadro constant (6.02 10^{23} mol^{-1}), e is the elementary charge (1.60 10^{-19} C) and I is the electrolyte ionic strength defined as in Equation 5:

$$I = \frac{1}{2}\sum_i z_i{}^2 C_i \qquad \text{Equation 5}$$

where z_i is the charge number of ion and C_i is its molar concentration. A λ_D value of 0.355 nm was calculated for the K_2SO_4 0.25 mol.L^{-1} aqueous electrolyte while 0.309 nm was found for KPF_6 0.5 mol.L^{-1} EC:DEC-based electrolyte. These values are significantly smaller than the respective penetration depths (189 and 225 nm). To fully relate these two variables, the velocity of the moving layer needs to be assessed at the extremity of the EDL. As depicted in Figure 3a, the velocity of the damped acoustic wave follows an exponential decay parallel to the surface normal, as (Equation 6):

$$v(x) = v_0 exp(-x/\delta) \qquad \text{Equation 6}$$

For both electrolytes, the $v(\lambda_D)/v_0$ ratio gives rise to the value of 0.998, meaning that any ions present in the EDL region are moving in phase with the

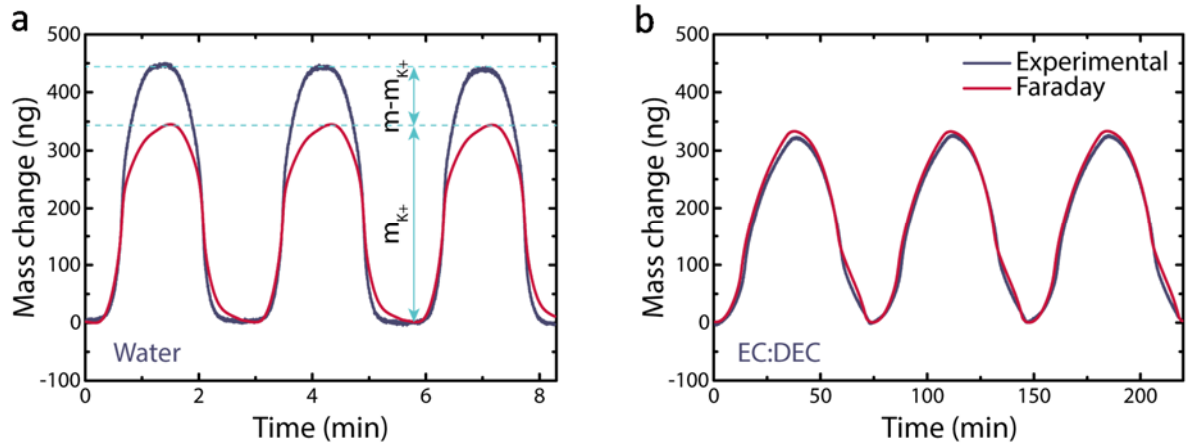

Figure 5. Experimental (EQCM) and electrochemical mass (Faraday) comparison calculated for a 100 nm thick film (a) in 0.25 mol.L^{-1} K_2SO_4 (pH 3.5) water-based electrolyte during a CV at 10 mV.s^{-1} and (b) in 0.5 mol.L^{-1} KPF_6 EC:DEC-based electrolyte during a CV at 0.5 mV.s^{-1}. The corresponding EQCM data are presented in Figure 2.

solid surface, even though they are not rigidly attached to it.[43] Therefore, according to the aforementioned analytical treatment, the ions fluxes and especially the desolvation process occurring in the close vicinity of the EDL contribute to the frequency change, are detected and quantifiable. Tsionsky and co-workers proposed the formation of a "viscous layer" in the EDL region on a flat surface.[43, 44] According to their studies, the accumulation of cations in this region due to the negative polarization causes an increase in the local viscosity, which can contribute to the frequency change. Their interpretation originates from the observation of a frequency shift of -5 Hz with a 6 MHz quartz resonator, corresponding to -11.3 Hz with the 9 MHz quartz resonators used in this study. Therefore, this contribution is negligible in the case of PB film with a relatively flat surface, especially when the difference between the experimental and theoretical frequency changes are around 100 Hz for the aqueous electrolyte and matching for non-aqueous ones. Moreover, no energy, *i.e.* no motional resistance change, is dissipated due to viscoelastic changes during the potassium insertion/extraction in our PB electrode (Figure 2, bottom panel). These results demonstrate that the desolvation process taking place at the interface is at the origin of the difference between theoretical and experimental frequency shifts (Figure 5a).

In summary, the analyses of the *operando* EQCM –R results have indicated the absence of organic solvent molecules in the environment of the potassium ions, whereas they are still partially hydrated (0.61 water molecules per K^+ obtained from Figure 5a) at the electrode-electrolyte interface and particularly in the EDL region. Note that water co-insertion was discarded in our explanatory, since there is no difference detected in potassium ions' solid diffusion coefficient between aqueous and non-aqueous electrolytes (Figure S2).

3.2.4. Final evidence of the involved species at the EEI and their associated interfacial kinetics:

i) Identification of the nature of species and their dynamics at EEI: At this stage, pairing EQCM with EIS measurement (the so-called *ac*-electrogravimetry) was used to deconvolute the complex insertion processes at the EEI by identifying the species by their molar mass, together with the respective kinetics of interfacial transfer. Alike typical EIS measurements, a suitable model for each system needs to be developed to extract parameters related to the interfacial transfer and the desolvation process. The model and the fitting methodology of the *ac*-electrogravimetric results have been previously described and briefly recalled in the Supplementary Information, part 8.[11, 22, 23]

Ac-electrogravimetric measurements were carried out at various stationary potentials in the same potential range used for the EQCM measurements (Figure 2), both in aqueous and non-aqueous electrolytes. The *ac*-electrogravimetric results obtained at -0.25 V *vs.* Hg/Hg_2SO_4 and 3.2 V *vs.* K^+/K^o are shown in Figure 6a,c and b,d, respectively. The charge/potential transfer function (TF), $\Delta q/\Delta E(\omega)$, has been presented instead of classical impedance representation (*i.e.* potential/current TF, $\Delta E/\Delta I(\omega)$) where the following relation exists between the two: $\frac{\Delta E}{\Delta I}(\omega) = R_{el} + \frac{1}{j\omega\left(C_{dl}+\frac{\Delta q}{\Delta E}(\omega)\right)}$ (with R_{el}: the electrolyte resistance and C_{dl}: the double layer capacitance). This representation is more convenient to decouple the contribution of charged species, as one loop corresponds to one charged species. For aqueous electrolyte, the collected spectrum of $\Delta q/\Delta E(\omega)$ at

-0.25 V *vs.* Hg/Hg_2SO_4 shows two loops implying that two charged species (ion 1 and ion 2) involved in the charge compensation process (Figure 6a). The experimental $\Delta q/\Delta E(\omega)$ TF was fitted with the theoretical equation given in Equation S12, involving two ionic species. A good agreement is found between the experimental and theoretical curve in Figure 6a, both in terms of shape and frequency distribution. The fitting parameters, K_i (kinetics of transfer) and G_i (related to interfacial transfer resistance), are obtained for the two ions. At this stage, it is not possible to identify these ionic

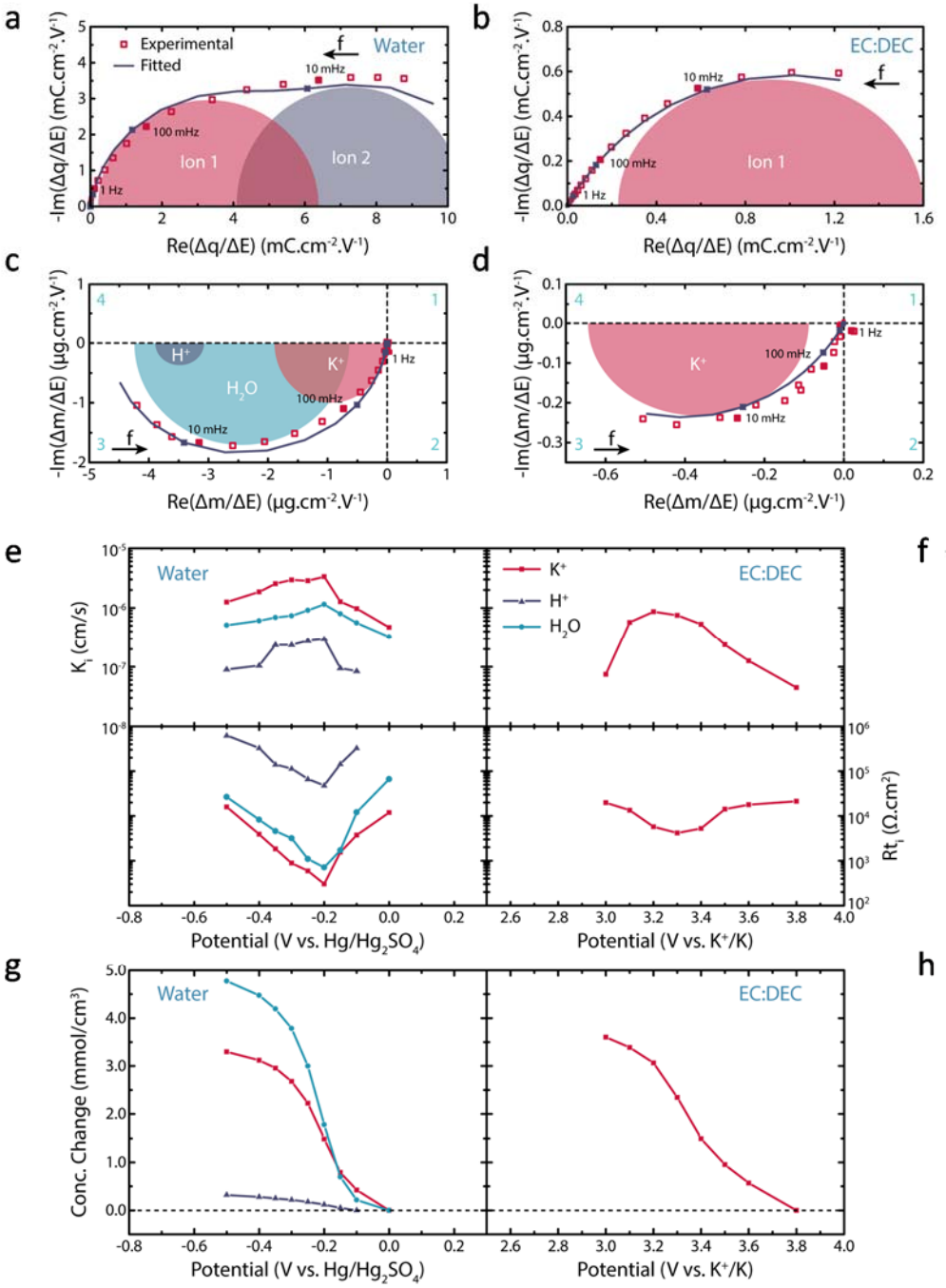

Figure 6. *Ac*-electrogravimetric analyses of 100 nm thick Prussian Blue films in (a,c) water and (b,d) EC:DEC-based electrolytes. (a,b) Charge/potential $\Delta q/\Delta E(\omega)$ and (c,d) mass/potential $\Delta m/\Delta E(\omega)$ transfer functions at -0.25 V *vs.* Hg/Hg_2SO_4 for aqueous electrolyte and at 3.2 V *vs.* K^+/K^o for non-aqueous electrolyte. Both experimental and theoretical curves are given. The different loops, which are drawn to guide the eye based on the fitting parameters, are labelled with the involved species. Evolution of kinetic parameters, K_i, (e, f top panels) and interfacial transfer resistances, $Rt_i = \frac{1}{FG_i}$, (e, f lower panels) and (g, h) relative concentration variation of each species, represented as a function of the potential.

contributions. Then, to identify and clarify the contribution of the charged and also uncharged species (free electrolyte molecules), the experimental mass/potential transfer function $\Delta m/\Delta E(\omega)$, the second main TF of the measurement is analyzed (Figure 6c). One big loop appears in the 3rd quadrant which is characteristic for cation contribution or free solvent molecules, transferred in the same flux direction as cations.[11, 22, 40] The mass/potential transfer function $\Delta m/\Delta E(\omega)$ is fitted using theoretical equation given in Equation S15. The K_i and G_i parameters for the charged species, previously estimated in the fitting of the $\Delta q/\Delta E(\omega)$ TF, are used. Three cationic species were considered to fit the mass/potential TF: K^+, H^+ and H_3O^+. Two possible couples were investigated, keeping in common K^+: K^+/H^+ and K^+/H_3O^+. Both have been tested to fit the mass/potential TF but neither of them were satisfactory due to the impossibility to fit the massive negative loop with the combination between their molar mass and their estimated fitting parameters K_i and G_i. Contribution from water molecules was thus injected into the model, allowing a better agreement between the fit and the experimental mass/potential TF. The different permutations of the listed species were considered and the two partial mass/potential TFs (Equation S17, a crosscheck procedure of the fitting described in the Supporting Information) were tested to further verify the unicity of the fitting parameters. In the end, only the model enlisting K^+, H_2O and H^+ at high, medium and low frequency, respectively, resulted in a satisfactory fit, in terms of shape and frequencies.

Concerning the *ac*-electrogravimetry in the non-aqueous medium, the same fitting protocol was performed. The collected spectrum of $\Delta q/\Delta E(\omega)$ at 3.2 V vs. K^+/K^o, represented in Figure 6b, shows only one loop implying that only one ion (ion 1) is involved in the interfacial process. One loop is also present in the 3rd quadrant of the mass/potential TF, demonstrating the participation of one cation or free solvent molecules in the same flux direction as the cation. Despite the measurement down to the LF range of about 1 mHz, the loops are not closed and do not form a complete semi-circle due to the instrumental and time limitations (2-3 h for each potential), demonstrating the slow kinetics of the interfacial ionic transfer. A model using one cation was employed to fit the experimental spectrum of charge/potential TF and obtain the kinetic parameter, K_i, and the inverse of the transfer resistance, G_i. A good agreement was obtained between the experimental and fitted curves in Figure 6b. These parameters were kept constant and potassium ions were assumed to be the sole involved species. In these terms, the experimental and theoretical mass/potential TFs match well without the addition of an additional contribution of an uncharged species (Figure 6d).

Thus, *ac*-electrogravimetry has demonstrated the sole contribution of potassium ions in the non-aqueous electrolyte. As for the aqueous electrolyte, the water molecules as well as protons (although their contribution is much lower than potassium species) are involved in the insertion mechanism of the potassium ions, at the EEI of the PB phase. These results are in a good agreement with classical EQCM measurements (Figure 2 and Figure 5).

ii) Study of the interfacial kinetics associated to the involved species: A similar fitting procedure described for the -0.25 V *vs.* Hg/Hg_2SO_4 and 3.2 V *vs.* K^+/K^o was carried out for all the other measurements performed in the potential range of both electrolytes. The contribution of the different involved species determined in the previous section (K^+, H^+ and H_2O) is found to be persistent at all the potentials studied. The obtained values and their dependency on the potential are shown in Figure 6e-f.

The *ac*-electrogravimetric analysis performed in water-based electrolyte shows that the interfacial kinetic of transfer, K_i , of the involved species is ranked as follows: $K^+ > H_2O > H^+$, independently of the potential. Their kinetics of transfer are quite steady over the potential window with a peak centered around the insertion/extraction redox potential and the water kinetics seem to follow potassium ions in terms of shape and values. Regarding the interfacial transfer resistance, Rt_i, a V-shaped response is found for each species. The minimum value of their resistance is yet again centered on the redox potential, in perfect agreement with the sharp and well-defined mass change response observed by EQCM in the Figure 2a middle panel. It can also be noted that the Rt_i values are 2-3 orders of magnitude higher in the case of H^+ compared to the two other species, demonstrating the difficulty of protons to be inserted into the PB structure. Concerning the non-aqueous electrolyte and the kinetic of potassium ions (Figure 6f, top), the peak shape is more pronounced and still centered on the redox potential. The lower K^+ kinetic of transfer values in non-aqueous electrolyte compared to aqueous counterpart explains the difference in rate capability. Moreover, the Rt_i as a function of potential shows a V-shape, but significantly broader in comparison to that obtained in aqueous electrolyte. This observation also explains the reason behind the more spread-out mass change over a larger potential window in the EQCM analyses (Figure 2b, middle panel).

The relative concentration variation of the three different species has been calculated from the *ac*-electrogravimetry analyses (Equation S18) and the results are represented in Figure 6g and h. Firstly, in

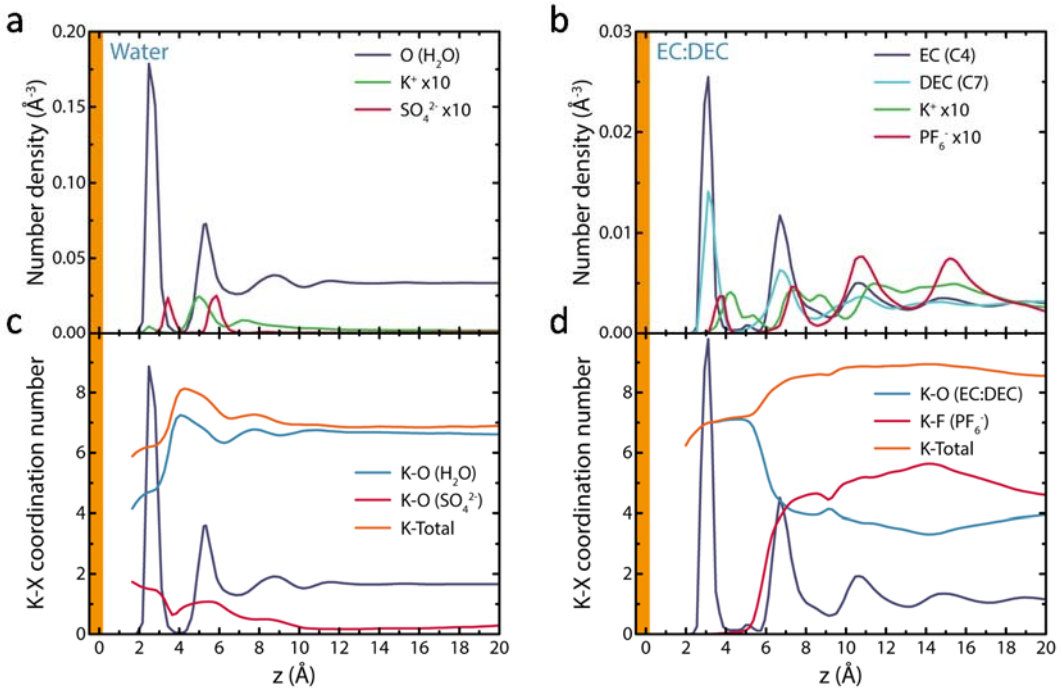

Figure 7. (a,b) Density profiles for ions and solvent molecules in the direction normal to the surface (z) for (a) 0.25 mol.L-1 K2SO4 in H2O and (b) 0.5 mol.L-1 KPF_6 in EC:DEC. C4 and C7 refer to the carbon atom of the carbonyl group for EC and DEC, respectively. Density profiles of the ions were multiplied by 10 because of their much lower concentrations with respect to the solvents (c,d) Evolution of the K-solvent, K-anion and K-Total (solvent + anion) coordination number as a function of the distance z from the surface (c) in water and (d) in EC:DEC. In the aqueous system, the O atom of H_2O and SO_4^{2-} have been considered. In the organic system, the carbonyl group oxygen atom of both EC and DEC is used to define the coordination number of the solvent, while the F atoms are considered for the anions. The density profiles of water and EC, and surface atoms are also plotted in panels (c) and (d). For all coordination numbers, the cut-off values correspond to the first minimum of the respective radial distribution functions.

aqueous electrolyte, the concentration variation of H^+ intervening in the insertion mechanism is highly negligible (which also corresponds to ~2.5 ng.cm^{-2}) in comparison with K^+ or H_2O contribution (~1248 and ~864 ng.cm^{-2}, respectively). The K^+ concentration variation is similar in both media with a sharper variation in aqueous electrolyte. The shape of the water contribution is following that of K^+ with a higher concentration variation. The concentration ratio between water and K^+ is equal to 1.4, which is higher than 0.61 water molecule per potassium ions evidenced in with $F\Delta m/\Delta Q$ measurement from CV at 10 mV.s^{-1} (Figure 5a). This discrepancy is most likely due to the way of measurement; *ac*-electrogravimetry provides a snapshot of the interface at quasi-equilibrium at the opposite of the CV.

Finally, in order to confirm the good exploitation of the *ac*-electrogravimetry fitting procedure, the global mass variation was recalculated from the concentration change of the different species involved and compared with the results obtained by EQCM in the Figure 2, middle panel. Such comparisons are plotted in Figure S7. These results nicely compare, hence validating the employed models and the described *ac*-electrogravimetric analyses, demonstrating the contribution of potassium ions solely in the non-aqueous electrolyte whereas potassium ions and water molecules acting as main species in the aqueous electrolyte.

3.3. Molecular picture from classical Molecular Dynamics simulations:

In order to rationalize our experimental findings and further understand the difference between the double layer formed at the electrode-electrolyte interfaces, the two liquids were simulated in contact with Au electrodes held at constant potential. Representative snapshots extracted from the MD simulations of K2SO4 in H2O and KPF_6 in EC/DEC are provided in Figure S8. The choice of this electrode, that is a nice example of flat metallic surface, was made because it is not possible to efficiently simulate insertion mechanisms using molecular dynamics. Figure 7 shows the density profiles in the direction normal to the surface (z) for K_2SO_4 in H_2O (Figure 7a) and KPF_6 in EC:DEC (Figure 7b). By focusing on the K^+ profiles (green), a marked difference can be seen in the way the

cations adsorb to the surface in the aqueous and non-aqueous solvent. In water a first small peak is found at about z = 2.5 Å, which corresponds to an inner-sphere adsorption, where K^+ cations are solvated within the topmost solvent layer in direct contact with the surface (inner Helmholtz plane (IHP) on Figure 3b). This is in line with the recent work of Li *et al.* evidencing the formation of a layer of water molecules in the IHP enhancing the surface diffusion of the cation to an insertion site.[45]

The second more intense peak at z = 5.0 Å corresponds instead to an outer-layer adsorption (at the frontier between the diffuse layer and the outer Helmholtz plane (OHP)). Strikingly, the inner-layer adsorption position is not observed for K^+ in the organic solvent, where the first peak in the cation profile is at about z = 4.5 Å, *i.e.* K^+ ions sit in the OHP and have a longer way to go for reaching the electrode. Its interaction with the organic solvent is weaker than with water, and since the former forms a very compact layer at the interface it is more difficult for the K^+ ions to reach the metal surface. Beyond the different adsorption position, the simulations reveal that the two solvents also offer a remarkably distinct coordination environment for the cations at the interface. Figure 7c,d show the evolution of the K-solvent and K-anion coordination numbers as a function of the distance z from the electrode in the two systems. In water, the strongest interaction is the one K^+ makes with H_2O and the K-H_2O coordination number shows only small variations for z > 4 Å, with an average coordination number in the bulk region of about 6.5. Only when K^+ faces the bare surface, water molecules start to leave the cation hydration layer, and they are partially replaced by SO_4^{2-} anions. In contrast, in the organic solvent K^+ interacts less strongly with the solvent and more strongly with the anions than it does in the aqueous system; the solvent and the anion almost equally populate the K^+ first coordination shell in the bulk (Figure 7d). When approaching the surface, the cations lose ion-pair interactions, which are replaced by weak interactions with the solvent. However, contrarily to the case of water, they still have a large barrier to cross (from the OHP to the IHP), which is consistent with the large contribution of the interfacial resistance evidenced by the *ac*-electrogravimetric experiments (Figure 6e-f). Indeed, higher interfacial resistance and lower interfacial kinetics of transfer values for the K^+ ions insertion at the electrode/electrolyte interface in nonaqueous medium than that occur in aqueous electrolyte is supported by MD simulations, showing a barrier of solvent molecules at the IHP. This barrier impedes the K^+ insertion kinetics and increase the activation energy in comparison with aqueous electrolyte. In addition, the interactions with the first adsorbed solvent layer are much weaker than in the case of water, which may explain why the organic solvent molecules do not contribute to the insertion mechanism. Using the same methodology, similar results have been obtained for 1M $LiClO_4$ in water and in propylene carbonate (PC) in contact with Au electrodes, with the Li^+ cations having a higher probability to populate the IHP in water than in PC (see Figure S9). In addition, as for K^+, their solvation number also tends to increase at the interface with the organic solvent while it is not the case in water. These theoretical findings are in agreement with the similar trend observed experimentally for the aqueous *vs.* non-aqueous insertion of K^+ into the Prussian blue phase $Fe_4^{III}[Fe^{II}(CN)_6]_3$ and Li into $LiFePO_4$.

4. CONCLUSIONS

In this work, we have investigated the mechanistic of the K^+ insertion process in the Prussian blue phase $Fe_4^{III}[Fe^{II}(CN)_6]_3$ as function of the aqueous and non-aqueous nature of the electrolyte. It should be underlined that drastic differences were found between both electrolyte media. To identify the origin of such differences, in-depth electrochemical analyses were performed to highlight the rate-limiting step of the insertion mechanism. First, PITT and Randles-Sevcik type analysis of CV responses have clearly shown that the potassium ions solid diffusion cannot be the limiting step. Moreover, they revealed a fast and unaltered charge transfer that do not affect the overall kinetics, hence calling for another explanation. Further, we demonstrated through electrogravimetric measurements the presence of an additional mass change compared to the theoretical mass uptake due to the sole potassium insertion, observed only in the aqueous media. Such an observation is commonly indicative of the contribution of a “viscous layer” but shown to be negligible compared with additional frequency change observed here. It can also be viewed as the viscoelastic change of the PB film upon cycling due to water co-insertion. However, such a hypothesis was eliminated by monitoring upon cycling, *via* EQCM-R, the motional resistance which reveals the absence of viscoelastic change during K^+ insertion in PB thin films. We equally discarded co-inserted water molecules since the solid diffusion coefficient was not affected when switching from organic to aqueous electrolyte. These results led us to hypothesize the participation of the solvent molecules during the cation insertion at the electrode-electrolyte interface, most likely localized in the electrochemical double layer region, that we unambiguously confirmed by *ac*-electrogravimetric analyses. The passing through a transition step, between solvated cation in the electrolyte and bare cation in the insertion material, where the cation is partially solvated at the interface was firstly introduced by Bruce and

Saidi,[46] and paved the way to new modelling of the interface.[47, 48] However, in contrast to Li-ion chemistry, no organic molecules were found in the close proximity of the potassium ion before its insertion. In addition, the difference in rate capability was confirmed by the kinetic study provided by *ac*-electrogravimetry.

The present study on K-ion (PB) chemistry and supported by our previous work on Li-ion[10] (LFP) demonstrated that in non-aqueous electrolytes, when using heavier alkali metals, the number of solvent molecules participating in the partial solvation shell at the interface decreases. At the same time, the desolvation energy in the bulk of the electrolyte decreases when moving from lithium to potassium ions, explaining the better rate capability. In contrast, this trend is not followed in water-based electrolytes, since the desolvation energy is always higher in aqueous electrolyte and yet exhibit better power performance. A partially hydrated cation (close transfer kinetics between the cation and solvent molecules) is always found in the electrochemical double layer region. As mentioned, facilitating the surface diffusion of a cation to an insertion site has been proposed to be correlated to the formation of a layer of water molecules in the IHP.[45] This phenomenon was demonstrated in non-aqueous electrolyte where water was used as an additive for Mg^{2+} insertion in WO_3.[49] Through molecular dynamics simulations of the double layer structure forming by the two liquids at a model flat electrode, we could indeed confirm that in water, some K^+ ions lie in the IHP but remain rather strongly solvated, hence explaining the contribution of water molecules in the insertion mechanism. In contrast, in the organic solvents, they adsorb in the OHP. The solvent molecules are *i)* weakly bond to the K^+, hence they do not participate to the adsorption and *ii)* forming a barrier at the surface of the electrode, which may explain the slower insertion kinetics in this system. Through investigation of two distinct alkali metal-ion chemistries (Li-ion[10] and herein K-ion), we explicitly demonstrate that the desolvation process occurring at the EEI is found to be the origin of the rate capability difference in aqueous and non-aqueous electrolytes. These studies provide a novel methodology for understanding the positional cohabitation of the cations and solvent molecules within the double layer structure forming at the electrode-interface. They also motivate for broader exploration of interface engineering *via* various salts and solvents to improve the power performances of batteries that were so far mainly believed to be dominated by the ionic conductivity of the electrolyte when comparing aqueous and non-aqueous electrolytes.

ASSOCIATED CONTENT

Supporting Information. Diffusion coefficient calculation details (employing PITT and Randles-Sevcik equation), rate capability difference in (non)aqueous electrolytes, further characterization of the PB films with different thickness, validation of the gravimetric sensing conditions for the electrogravimetric studies, theoretical background for *ac*-electrogravimetry measurements. Classical molecular dynamics simulations details and density profile results for 1M $LiClO_4$ in H_2O and PC.

AUTHOR INFORMATION

Corresponding Authors

* Jean-Marie Tarascon - Chimie du Solide et de l'Energie, UMR 8260, Collège de France, 11 Place Marcelin Berthelot, 75231 Paris Cedex 05, France; orcid.org/0000-0002-7059- 6845; E-mail: jean-marie.tarascon@college-de-france.fr

* Ozlem Sel - Chimie du Solide et de l'Energie, UMR 8260, Collège de France, 11 Place Marcelin Berthelot, 75231 Paris Cedex 05, France; orcid.org/0000-0002-8501-4561; E-mail: ozlem.sel@sorbonne-universite.fr

Notes

The authors declare no competing financial interest.

ACKNOWLEDGEMENTS

J.-M.T. and P.L. acknowledge funding from the European Research Council (ERC) (no. FP/2014)/ERC; grant project no. 670116-ARPEMA). A.S. and M.S. acknowledge funding from the European Research Council under the European Union's Horizon 2020 research and innovation program (grant agreement no. 771294). This work was supported by the French National Research Agency (Labex STORE-EX, Grant ANR-10-LABX-0076). The authors acknowledge HPC resources granted by GENCI (resources of IDRIS, Grant No. A0100910463). FEGSEM & EDX instrumentation was hosted at the Institut des Matériaux de Paris Centre (no. IMPCFR2482) and was funded by Sorbonne Université, CNRS and by the C'Nano projects of the Région Ile-de-France.

REFERENCES

1. Yamada, Y.; Wang, J.; Ko, S.; Watanabe, E.; Yamada, A., Advances and Issues in Developing Salt-Concentrated Battery Electrolytes. *Nat. Energy* **2019,** *4* (4), 269.

2. Hwang, S.; Kim, D.-H.; Shin, J. H.; Jang, J. E.; Ahn, K. H.; Lee, C.; Lee, H., Ionic Conduction and Solution Structure in $LiPF_6$ and LiBF4 Propylene Carbonate Electrolytes. *J. Phys. Chem. C* **2018,** *122* (34), 19438.

3. Hall, D. S.; Eldesoky, A.; Logan, E. R.; Tonita, E. M.; Ma, X.; Dahn, J. R., Exploring Classes of Co-Solvents for Fast-Charging Lithium-Ion Cells. *J. Electrochem. Soc.* **2018,** *165* (10), A2365.

4. Uchida, S.; Ishikawa, M., Lithium bis(fluorosulfonyl)imide based Low Ethylene Carbonate Content Electrolyte with Unusual Solvation State. *J. Power Sources* **2017,** *359*, 480.

5. Kubota, K.; Dahbi, M.; Hosaka, T.; Kumakura, S.; Komaba, S., Towards K-Ion and Na-Ion Batteries as "Beyond Li-Ion". *Chem. Rec.* **2018,** *18* (4), 459.

6. Jun, M. M.; Shik, J. M., The Studies on the Hydration Energy and Water Structures in Dilute Aqueous Solution. *Bull. Chem. Soc. Jpn.* **1986,** *59* (4), 1215.
7. Bai, P.; Bazant, M. Z., Charge Transfer Kinetics at the Solid–Solid Interface in Porous Electrodes. *Nat. Commun.* **2014,** *5* (1), 3585.
8. Chekushkin, P. M.; Merenkov, I. S.; Smirnov, V. S.; Kislenko, S. A.; Nikitina, V. A., The Physical Origin of the Activation Barrier in Li-Ion Intercalation Processes: The Overestimated Role of Desolvation. *Electrochim. Acta* **2021,** *372*, 137843.
9. Nikitina, V. A.; Zakharkin, M. V.; Vassiliev, S. Y.; Yashina, L. V.; Antipov, E. V.; Stevenson, K. J., Lithium Ion Coupled Electron-Transfer Rates in Superconcentrated Electrolytes: Exploring the Bottlenecks for Fast Charge-Transfer Rates with LiMn2O4 Cathode Materials. *Langmuir* **2017,** *33* (37), 9378.
10. Lemaire, P.; Dargon, T.; Alves Dalla Corte, D.; Sel, O.; Perrot, H.; Tarascon, J.-M., Making Advanced Electrogravimetry as an Affordable Analytical Tool for Battery Interface Characterization. *Anal. Chem.* **2020,** *92* (20), 13803.
11. Gabrielli, C.; García-Jareño, J. J.; Keddam, M.; Perrot, H.; Vicente, F., Ac-Electrogravimetry Study of Electroactive Thin Films. I. Application to Prussian Blue. *J. Phys. Chem B* **2002,** *106* (12), 3182.
12. Yagi, S.; Fukuda, M.; Makiura, R.; Ichitsubo, T.; Matsubara, E., EQCM Analysis of Redox Behavior of Prussian Blue in a Lithium Battery Electrolyte. *J. Mater. Chem. A* **2014,** *2* (21), 8041.
13. Saeed, S.; Boyd, S.; Tsai, W.-Y.; Wang, R.; Balke, N.; Augustyn, V., Understanding Electrochemical Cation Insertion into Prussian Blue from Electrode Deformation and Mass Changes. *Chem. Commun.* **2021,** *57* (55), 6744.
14. Zhang, C.; Xu, Y.; Zhou, M.; Liang, L.; Dong, H.; Wu, M.; Yang, Y.; Lei, Y., Potassium Prussian Blue Nanoparticles: A Low-Cost Cathode Material for Potassium-Ion Batteries. *Adv. Funct. Mater.* **2017,** *27* (4), 1604307.
15. Mathew, V.; Kim, S.; Kang, J.; Gim, J.; Song, J.; Baboo, J. P.; Park, W.; Ahn, D.; Han, J.; Gu, L.; Wang, Y.; Hu, Y.-S.; Sun, Y.-K.; Kim, J., Amorphous Iron Phosphate: Potential Host for Various Charge Carrier Ions. *NPG Asia Mater.* **2014,** *6* (10), e138.
16. Itaya, K.; Akahoshi, H.; Toshima, S., Electrochemistry of Prussian Blue Modified Electrodes: An Electrochemical Preparation Method. *J. Electrochem. Soc.* **1982,** *129* (7), 1498.
17. Mortimer, R. J.; Rosseinsky, D. R., Iron Hexacyanoferrate Films : Spectroelectrochemical Distinction and Electrodeposition Sequence of 'Soluble' (K^+-Containing) and 'Insoluble' (K^+-Free) Prussian Blue, and Composition Changes in Polyelectrochromic Switching. *J. Chem. Soc., Dalton Trans.* **1984,** (9), 2059.
18. Rietveld, H., A Profile Refinement Method for Nuclear and Magnetic Structures. *J. Appl. Crystallogr.* **1969,** *2* (2), 65.
19. Rodríguez-Carvajal, J., Recent Advances in Magnetic Structure Determination By Neutron Powder Diffraction. *Physica B: Condens. Matter.* **1993,** *192* (1), 55.
20. Momma, K.; Izumi, F., VESTA 3 for Three-Dimensional Visualization of Crystal, Volumetric and Morphology data. *J. Appl. Crystallogr.* **2011,** *44* (6), 1272.
21. Sauerbrey, G., Verwendung von Schwingquarzen zur Wägung dünner Schichten und zur Mikrowägung. *Z. Phys. B: Condens. Matter* **1959,** *155* (2), 206.
22. Arias, C. R.; Debiemme-Chouvy, C.; Gabrielli, C.; Laberty-Robert, C.; Pailleret, A.; Perrot, H.; Sel, O., New Insights into Pseudocapacitive Charge-Storage Mechanisms in Li-Birnessite Type MnO2 Monitored by Fast Quartz Crystal Microbalance Methods. *J. Phys. Chem. C* **2014,** *118* (46), 26551.
23. Escobar-Teran, F.; Perrot, H.; Sel, O., Charge Storage Properties of Single Wall Carbon Nanotubes/Prussian Blue Nanocube Composites Studied by Multi-Scale Coupled Electrogravimetric Methods. *Electrochim. Acta* **2018,** *271*, 297.
24. Marin-Laflèche, A. H., M.; Scalfi, L.; Coretti, A.; Dufils, T.; Jeanmairet, G.; Reed, S. K.; Serva, A.; Berthin, R.; Bacon, C.; Bonella, S.; Rotenberg, B.; Madden, P. A.; Salanne, M., MetalWalls: A Classical Molecular Dynamics Software Dedicated to the Simulation of Electrochemical Systems. *J. Open Source Softw.* **2020,** *5* (53), 2373.
25. Berendsen, H. J. C.; Grigera, J. R.; Straatsma, T. P., The Missing term in Effective Pair Potentials. *J. Phys. Chem.* **1987,** *91* (24), 6269.
26. Jorgensen, W. L.; Maxwell, D. S.; Tirado-Rives, J., Development and Testing of the OPLS All-Atom Force Field on Conformational Energetics and Properties of Organic Liquids. *J. Am. Chem. Soc.* **1996,** *118* (45), 11225.
27. Chaudhari, M. I.; Nair, J. R.; Pratt, L. R.; Soto, F. A.; Balbuena, P. B.; Rempe, S. B., Scaling Atomic Partial Charges of Carbonate Solvents for Lithium Ion Solvation and Diffusion. *J. Chem. Theory Comput.* **2016,** *12* (12), 5709.
28. Yu, H.; Whitfield, T. W.; Harder, E.; Lamoureux, G.; Vorobyov, I.; Anisimov, V. M.; MacKerell, A. D.; Roux, B., Simulating Monovalent and Divalent Ions in Aqueous Solution Using a Drude Polarizable Force Field. *J. Chem. Theory Comput.* **2010,** *6* (3), 774.
29. Pegado, L.; Marsalek, O.; Jungwirth, P.; Wernersson, E., Solvation and Ion-pairing Properties of the Aqueous Sulfate Anion: Explicit versus Effective Electronic Polarization. *Phys. Chem. Chem. Phys.* **2012,** *14* (29), 10248.
30. Canongia Lopes, J. N.; Deschamps, J.; Pádua, A. A. H., Modeling Ionic Liquids Using a Systematic All-Atom Force Field. *J. Phys. Chem B* **2004,** *108* (6), 2038.
31. Heinz, H.; Vaia, R. A.; Farmer, B. L.; Naik, R. R., Accurate Simulation of Surfaces and Interfaces of Face-Centered Cubic Metals Using 12–6 and 9–6 Lennard-Jones Potentials. *J. Phys. Chem. C* **2008,** *112* (44), 17281.
32. Serva, A.; Scalfi, L.; Rotenberg, B.; Salanne, M., Effect of the Metallicity on the Capacitance of Gold–aqueous Sodium Chloride Interfaces. *J. Chem. Phys.* **2021,** *155* (4), 044703.
33. García-Jareño, J. J.; Sanmatías, A.; Vicente, F.; Gabrielli, C.; Keddam, M.; Perrot, H., Study of Prussian Blue (PB) films by ac-electrogravimetry: influence of PB morphology on ions movement. *Electrochim. Acta* **2000,** *45* (22), 3765.
34. Hwang, J.-Y.; Myung, S.-T.; Sun, Y.-K., Recent Progress in Rechargeable Potassium Batteries. *Adv. Funct. Mater.* **2018,** *28* (43), 1802938.
35. Keiji Kanazawa, K.; Gordon, J. G., The Oscillation Frequency of a Quartz Resonator in Contact With Liquid. *Anal. Chim. Acta* **1985,** *175*, 99.
36. Levi, M. D.; Salitra, G.; Levy, N.; Aurbach, D.; Maier, J., Application of a Quartz-Crystal Microbalance to Measure Ionic Fluxes in Microporous Carbons for Energy Storage. *Nat. Mater.* **2009,** *8* (11), 872.
37. García-Jareño, J. J.; Gabrielli, C.; Perrot, H., Validation of the Mass Response of a Quartz Crystal Microbalance Coated with Prussian Blue Film for Ac Electrogravimetry. *Electrochem. Commun.* **2000,** *2* (3), 195.
38. Waegele, M. M.; Gunathunge, C. M.; Li, J.; Li, X., How Cations Affect the Electric Double Layer and The Rates and Selectivity of Electrocatalytic Processes. *J. Chem. Phys.* **2019,** *151* (16), 160902.
39. Xu, K.; von Wald Cresce, A., Li^+-Solvation/Desolvation Dictates Interphasial Processes on Graphitic Anode in Li Ion Cells. *J. Mater. Res.* **2012,** *27* (18), 2327.
40. Kim, L. T. T.; Gabrielli, C.; Perrot, H.; Garcia-Jareno, J.; Vicente, F., Redox Switching of Prussian Blue Thin

Films Investigated by Ac-electrogravimetry. *Electrochim. Acta* **2012,** *84*, 35.
41. Wang, F.; Varenne, F.; Ortiz, D.; Pinzio, V.; Mostafavi, M.; Le Caër, S., Degradation of an Ethylene Carbonate/Diethyl Carbonate Mixture by Using Ionizing Radiation. *ChemPhysChem* **2017,** *18* (19), 2799.
42. Naejus, R.; Damas, C.; Lemordant, D.; Coudert, R.; Willmann, P., Excess Thermodynamic Properties of the Ethylene Carbonate–Trifluoroethyl Methyl Carbonate and Propylene Carbonate–Trifluoroethyl Methyl Carbonate Systems at T= (298.15 or 315.15) K. *J. Chem. Thermodyn.* **2002,** *34* (6), 795.
43. Tsionsky, V.; Daikhin, L.; Gileadi, E., Weighing Ions in Solution with the Quartz Crystal Microbalance. *J. Electrochem. Soc.* **1995,** *142* (12), L233.
44. Tsionsky, V.; Daikhin, L.; Gileadi, E., Response of the Electrochemical Quartz Crystal Microbalance for Gold Electrodes in the Double-Layer Region. *J. Electrochem. Soc.* **1996,** *143* (7), 2240.
45. Li, Y.; Chen, H.; Lim, K.; Deng, H. D.; Lim, J.; Fraggedakis, D.; Attia, P. M.; Lee, S. C.; Jin, N.; Moškon, J.; Guan, Z.; Gent, W. E.; Hong, J.; Yu, Y.-S.; Gaberšček, M.; Islam, M. S.; Bazant, M. Z.; Chueh, W. C., Fluid-enhanced Surface Diffusion Controls Intraparticle Phase Transformations. *Nat. Mater.* **2018,** *17* (10), 915.
46. Bruce, P. G.; Saidi, M. Y., The Mechanism of Electrointercalation. *J. Electroanal. Chem.* **1992,** *322* (1), 93.
47. Lück, J.; Latz, A., Theory of Reactions at Electrified Interfaces. *Phys. Chem. Chem. Phys.* **2016,** *18* (27), 17799.
48. Lück, J.; Latz, A., Modeling of the Electrochemical Double Layer and Its Impact on Intercalation Reactions. *Phys. Chem. Chem. Phys.* **2018,** *20* (44), 27804.
49. Wang, R.; Boyd, S.; Bonnesen, P. V.; Augustyn, V., Effect of Water in a Non-aqueous Electrolyte on Electrochemical Mg^{2+} Insertion into WO_3. *J. Power Sources* **2020,** *477*, 229015.

Table of Contents (TOC Graphic)

Investigation of two distinct alkali metal-ion chemistries (K-ion but also Li-ion) reveals the desolvation process occurring at the electrode interface to be the origin of the rate capability difference in aqueous and non-aqueous electrolytes. Tailoring this interface structuring *via* the proper salt-solvent interaction is the key to enabling the best power performances in alkali metal-ion batteries.

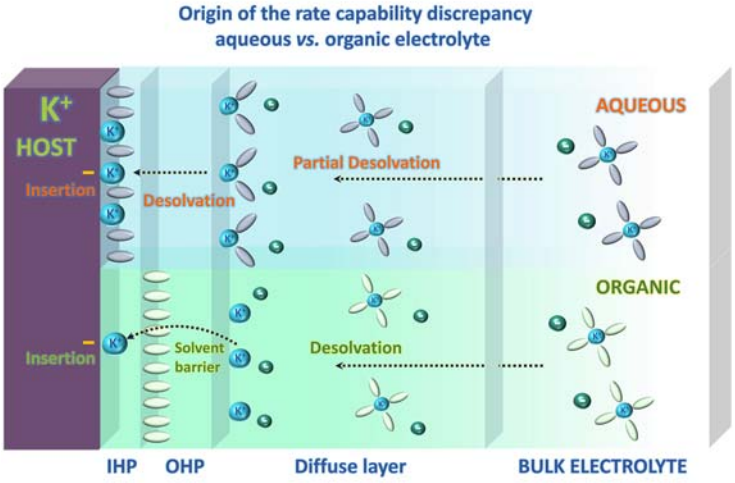

Supporting Information For

Probing the Electrode-Electrolyte Interface of a Model K-ion Battery Electrode – the Origin of Rate Capability Discrepancy Between Aqueous and Non-Aqueous Electrolytes

Pierre Lemaire[†,‡,§], Alessandra Serva[□], Mathieu Salanne[□,□], Gwënaelle Rousse,[†,‡,§,□], Hubert Perrot[¦], Ozlem Sel[†,§,*] and Jean-Marie Tarascon[†,§,*]

[†] Chimie du Solide et de l'Energie, UMR 8260, Collège de France, 11 Place Marcelin Berthelot, 75231 Paris Cedex 05, France

[‡] Sorbonne Université, 4 Place Jussieu, 75005 Paris, France

[§] Réseau sur le Stockage Electrochimique de l'Energie (RS2E), CNRS FR 3459, 33 Rue Saint Leu, 80039 Amiens Cedex, France

[□] Sorbonne Université, CNRS, Physico-chimie des Électrolytes et Nanosystèmes Interfaciaux, PHENIX, F-75005 Paris

[□] Institut Universitaire de France (IUF), 75231 Paris Cedex 05, France

[¦] Sorbonne Université, CNRS, Laboratoire Interfaces et Systèmes Electrochimiques, LISE, UMR 8235, 4 Place Jussieu, 75005 Paris, France

Corresponding authors:
Ozlem Sel: ozlem.sel@sorbonne-universite.fr
Jean-Marie Tarascon: jean-marie.tarascon@college-de-france.fr

1. Diffusion coefficient by PITT analyses

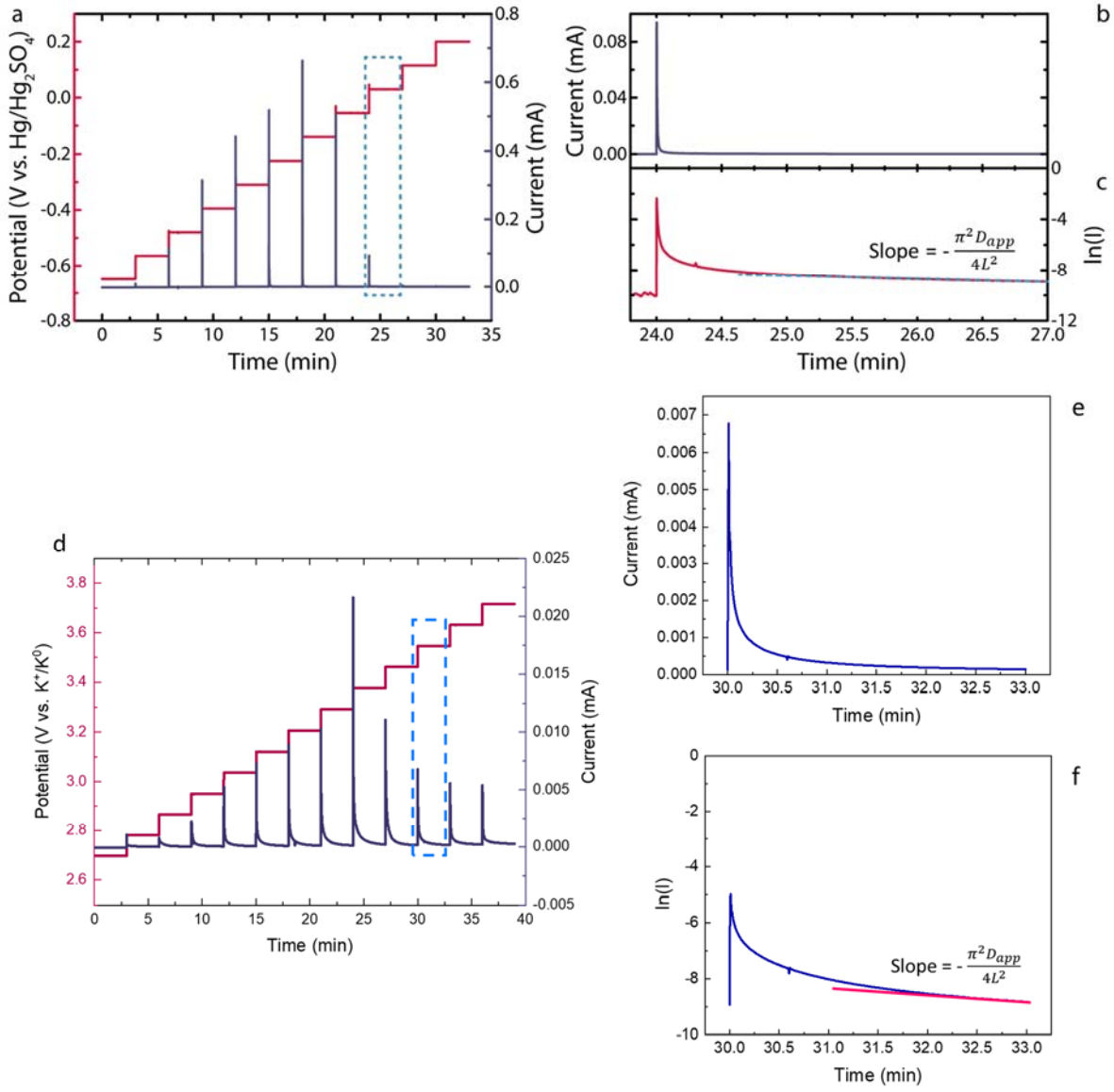

Figure S1. Apparent coefficient diffusion determination by PITT of K^+ in Prussian Blue film (100 nm) in K_2SO_4 0.25 mol.L^{-1} aqueous electrolyte. (a) Applied potential staircases and current response of the system. Focus on (b) the current response and (c) the natural logarithm of the current response for the 0.030 V vs. Hg/Hg_2SO_4 staircase. The panels d, e and f are the corresponding data in 0.5 mol.L^{-1} KPF_6 in EC:DEC. (d) Applied potential staircases and current response of the system. Focus on (e) the current response and (f) the natural logarithm of the current response for the 3.55 V vs. K^+/K^0 staircase.

Potentiostatic Intermittent Titration Technique (PITT): The PITT procedure is based on a staircase potential signal applied to the system, as represented in **Fig. S1**. In the case of a planar

electrode, Montella demonstrated that the current response of the system is dictated by the well known Cottrell relationship for short times and an exponential decay of diffusion current with respect to time for long times, if a restricted diffusion condition and diffusion control (very fast insertion reaction kinetics) are assumed.[1]

For short times, *i.e.* $t \ll \frac{L^2}{\pi^2 D_{app}}$,

$$I_d(t)_{st} = I_{Cottrell}(t) = -\frac{FA\sqrt{D_{app}{}'}\Delta c}{\sqrt{\pi}t} \qquad \textbf{(Equation S1)}$$

For long times, *i.e.*, $t \gg \frac{L^2}{\pi^2 D_{app}}$,

$$I_d(t)_{lt} = 2FA\frac{D_{app}}{L}\Delta c\ exp\left(-\frac{\pi^2 D_{app}}{4L^2}t\right) \qquad \textbf{(Equation S2)}$$

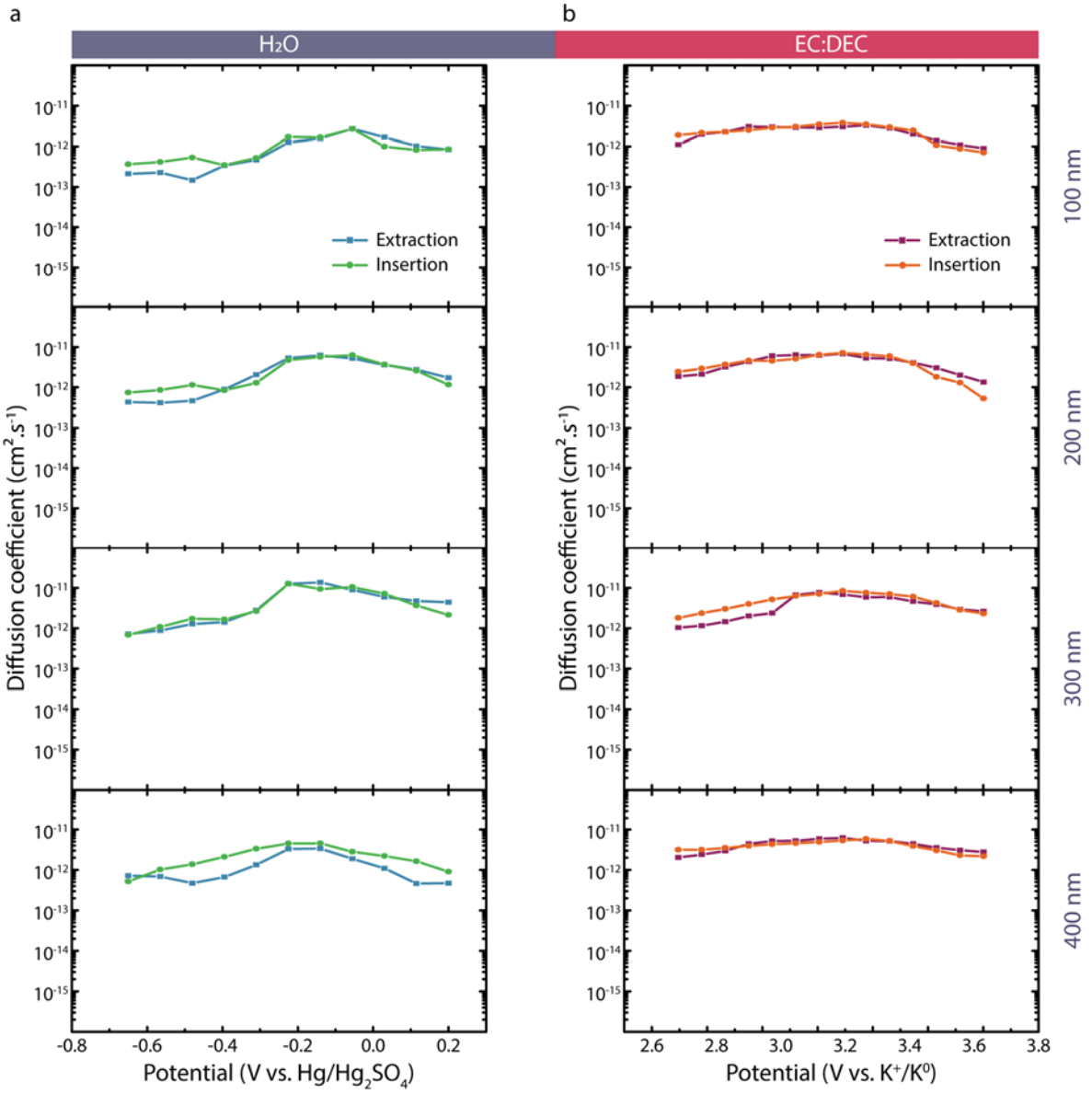

Figure S2. Solid diffusion coefficient determination of potassium ion in the bulk of the PB phase for different thicknesses in (a) water-based and (b) EC:DEC-based electrolytes.

where F is the Faraday's constant (96485 C.mol^{-1}), A is the specific surface are (0.196 cm²), Δc is the concentration variation in the film (mol.cm^{-3}), L is the film thickness (cm) and $D_{app}{}'$ is the apparent diffusion coefficient in the solid phase (cm².s^{-1}).

Then, the apparent diffusion coefficient can be extracted from slope of the natural logarithm of the **Equation S2** (**Fig. S1b** and **1c**), as it is independent of unknown variables.

$$ln(I_d(t)_{lt}) = ln\left(2FA\frac{D_{app}}{L}\Delta c\right) - \frac{\pi^2 D_{app}}{4L^2}t \qquad \textbf{(Equation S3)}$$

This procedure permits to obtain the apparent diffusion coefficient of the inserted cation in the solid phase at different potentials.

2. Diffusion coefficient by Randles-Sevcik equation

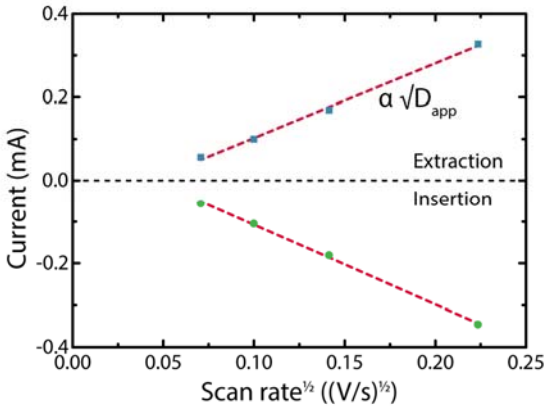

Figure S3. Apparent diffusion coefficient determination of K^+ during insertion and extraction in a Prussian Blue film (100 nm) in K_2SO_4 0.25 mol.L^{-1} aqueous electrolyte by the Randles-Sevcik equation.

Randles-Sevcik equation: The apparent diffusion coefficient of the inserted cation in the solid phase can also be estimated by the Randles-Sevcik equation. To fulfill the conditions of validity of this equation, the diffusion length of the inserted cation within the host material needs to be much smaller than the smallest dimension of the material such that the cation gradient can be considered as a semi-infinite linear diffusion-like process normal to the material interface. Then, assuming a Nernstian redox reaction (*i.e.* a fast reversible electron transfer reaction), the absolute current peak value has a linear relationship (in oxidation and reduction) to the square root of the scan rate of the cyclic voltammetry, following this equation:[2]

$$I_p = 0.4463\,FS\sqrt{\frac{F}{RT}}\frac{S_e}{S}\sqrt{D_{app}}xC_{mat}\nu^{1/2} \qquad \textbf{(Equation S4)}$$

where F is the Faraday's constant (96485 C.mol^{-1}), R is the gas constant (J.K^{-1}.mol^{-1}), T is the temperature (K), S_e and S are the specific surface and geometric area, respectively (cm²), x is the maximal mole fraction of inserted cation that can be inserted in the host material, C_{mat} is the concentration of the host material (mol.cm^{-3}), ν is the scan rate (V.s^{-1}), I_p is the value of the current peak (A) and D_{app} is the apparent diffusion coefficient of the inserted cation in the solid phase (cm².s^{-1}). An example of this procedure is represented in **Fig. S3**. It is emphasized that a fair similarity was found between the measured and theoretical masses and thicknesses of films below 300 nm, as represented in the **Fig. S4 b** and **d,** which demonstrates the negligible porosity of the PB films. Therefore, the film thickness is assumed as the shortest length for the Randles-Sevcik equation.

3. Condition for gravimetric sensing

Small variation of the motional resistance upon cycling means the retention of the rigid properties of the layers deposited on the conducting electrode of the quartz resonators. To go further in the analyses, the motional resistance can be converted to resonance width, W, thanks to the following equation:[3]

$$W = \frac{32Ae_{26}{}^2\rho_q{}^2f_0{}^3}{\pi\sqrt{\mu_q\rho_q}^3}R \qquad \textbf{(Equation S5)}$$

where e_{26} is the piezoelectric stress coefficient (9.65 10^{-2} A.s.m^{-2} for AT-cut quartz). In comparison to R, W has the unit of frequency (Hz) so it can be related to the resonance frequency change. The condition of the gravimetric sensing is defined as: $|\Delta W| \ll |\Delta f|$.

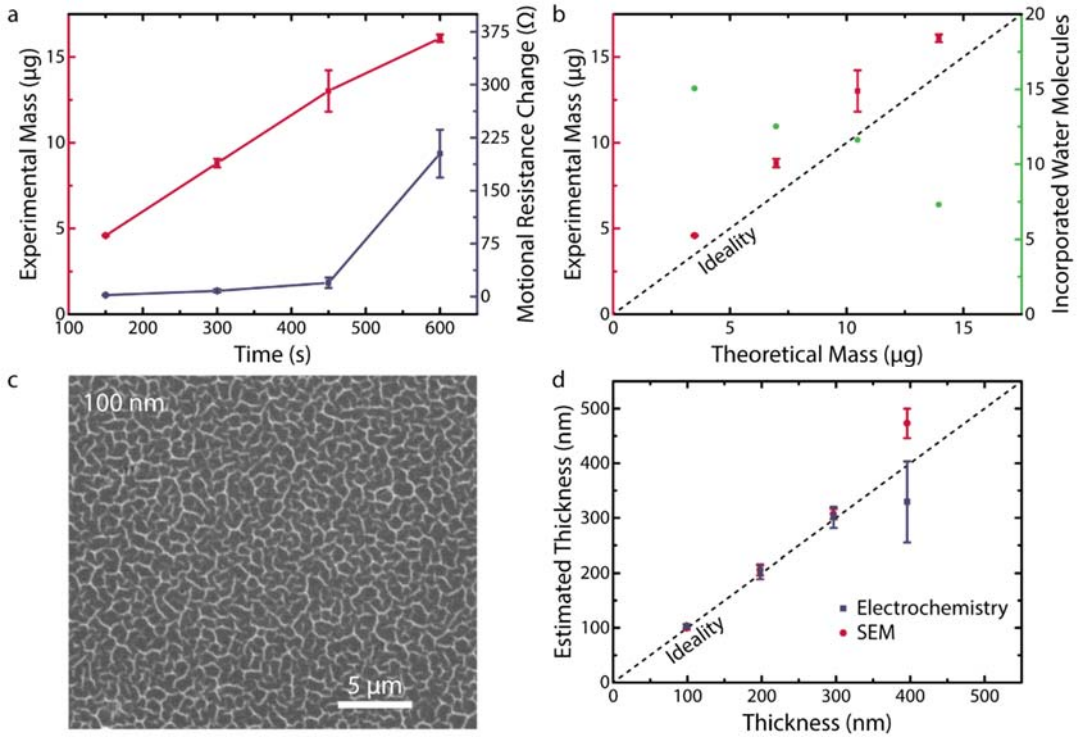

Fig. S4. (a) Experimental mass and motional resistance for PB films, measured in air. (b) Comparison of the experimental and the theoretical mass of the PB films and the respective number of associated incorporated water molecules. PB films with four different thicknesses, obtained at t_{ED} = 150, 300, 150 and 600s, are presented. (c) FEG-SEM image of a PB film surface with a nominal film thickness of 100 nm. (d) Comparison of the estimated and theoretical thicknesses of PB films by FEG-SEM and electrochemistry.

4. Water incorporation in the structure lattice

QCM with motional resistance monitoring enabled the estimation of the incorporated water in the structure lattice. To do so, the frequency and the motional resistance (R_m) of the resonators, before and after PB electrodeposition, were measured in air. The frequency changes were converted to the mass changes using Sauerbrey equation,[4] and allowed the experimental value of the electrodeposited PB mass to be estimated. The **Fig. S4a** shows that the experimental mass is linear with the electrodeposition time. The electrodeposited films, at least in the t_{ED} range of $150 \leq t_{ED} \leq 600$ s, do not show any indication of electronic conductivity loss, supported by the absence of a plateau in the experimental mass vs. t_{ED} plot in **Fig. S4a**. On the other hand, the R_m seems to exhibit a threshold for the films generated with a t_{ED} of more than 450 s, and a R_m value that increases drastically at t_{ED} of 600 s. It is noted that before this threshold value, the motional resistance is very low (< 30 Ω, for $t_{ED} \leq 450$ s) and falls within the suitable range for conducting electrochemical-gravimetric measurements. Even though the film obtained at t_{ED} = 600 s demonstrates a significant increase in the motional resistance, the $|\Delta W| \ll |\Delta f|$

condition for meaningful gravimetric sensing (**Equation S5**) is still fulfilled. *In situ* hydrodynamic spectroscopy was not performed for these coatings, considering the significantly low motional resistance values for $t_{ED} \leq 450$ s and the morphological features of the coatings (flat surface, low roughness).

The experimental mass of the electrodeposited PB films obtained from QCM measurements were compared to their theoretical counterparts (estimated by the Faraday's law). The **Fig. S4b** reveals a clear difference between these two set of values. For each film thicknesses, the experimental mass is slightly higher than the theoretical value. This phenomenon was already encountered by Buser *et al.* who provided evidence for the incorporation of between 14 and 16 water molecules into the unit cell.[5] For the films obtained at $t_{ED} \leq 450$ s, our results corroborated these values. Powder neutron diffraction demonstrated that 6 water molecules are coordinated to Fe^{III} at empty nitrogen sites and the remaining are present either as isolated molecules at the center of the unit cell or as water molecules hydrogen bonded to the coordinated ones.[6] For the EQCM tests in non-aqueous electrolyte (0.5 mol.L^{-1} KPF_6 in 50:50 ethylene carbonate (EC) and diethyl carbonate (DEC)), the films were dried under vacuum overnight at 80 °C. There was not any noticeable effect of the structural water neither upon immersion in the electrolyte (frequency response of the EQCM) nor during cycling in non-aqueous electrolytes.

5. Thickness control of the prepared films

The thickness of the electrodeposited films was estimated by two techniques. To begin with, cross section FEG-SEM images of the coatings were examined to measure its thickness at different spots of the sample, as represented in the **Fig. S4c**. For the sake of comparison, the film thickness was also estimated *via* electrochemistry. The films obtained with 4 different t_{ED} were cycled 15 times in aqueous medium containing 0.25 mol.L^{-1} K_2SO_4 at pH 3.5 to insert potassium ions in the structure, by leaching one iron during the first cycles, as described in the following equation:

$$Fe_4{}^{III}[Fe^{II}(CN)_6]_3 + 3\,K^+ = 3\,KFe^{III}[Fe^{II}(CN)_6] + Fe^{3+} \qquad \textbf{(Equation S6)}$$

In the following cycles, the potassium ions are reversibly inserted and extracted from the structure, as depicted in the following:

$$KFe^{III}[Fe^{II}(CN)_6] + K^+ + e^- = K_2Fe^{II}[Fe^{II}(CN)_6] \qquad \textbf{(Equation S7)}$$

The quantity of potassium ions stored into the structure was assessed thanks to the charge passing through the system upon oxidation. Then, using the following equation, the thicknesses of four different films can be estimated:

$$t_{film} = \frac{Q_{ox} N_A d^3}{4FS} \quad \textbf{(Equation S8)}$$

where Q_{ox} is the measured charge in oxidation (C), N_A is the Avogadro constant (6.02 10^{23} mol^{-1}), d is the characteristic distance of the PB unit cell, estimated earlier by Rietveld refinement (1.01 nm), 4 is the effective iron atoms in each unit cell, F is the Faraday's constant (96485 $C.mol^{-1}$) and S is the specific surface area, assimilated to the geometric surface thanks to the film flatness (0.196 cm^2).

The **Fig. S4d** gathers the thicknesses estimated by these two techniques and compares them with the theoretical ones. The **Fig. S4d** suggests a good agreement between the measured thicknesses and the theoretical ones for $t_{film} \leq 300$ nm. For the film of theoretically 400 nm, SEM cross section demonstrates that the film is thicker. However, the electrochemistry displays a lower value of the thickness, which means that part of this film is electrochemically inactive. These characterizations, besides confirming a true Prussian Blue phase formation at the surface of the gold patterned quartz resonator, also permitted the optimization of the PB thin films for the EEI study by electrochemical and electrogravimetric analyses. The films with nominal thicknesses ≤ 300 nm are suitable, evidenced by their low motional resistance change with respect to their loadings and the morphological features (*i.e.* flat surface).

6. Rate capability difference of PB thin films in aqueous and organic electrolyte

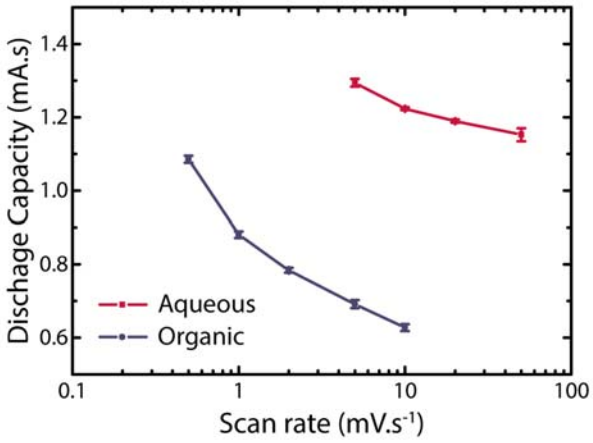

Figure S5. Rate capability assessment of the 100 nm thick PB film in aqueous (0.25 mol.L^{-1} K_2SO_4 in H_2O (pH 3.5)) and non-aqueous electrolyte (0.5 mol.L^{-1} KPF_6 in EC:DEC) by means of the discharge capacity.

7. EQCM analyses

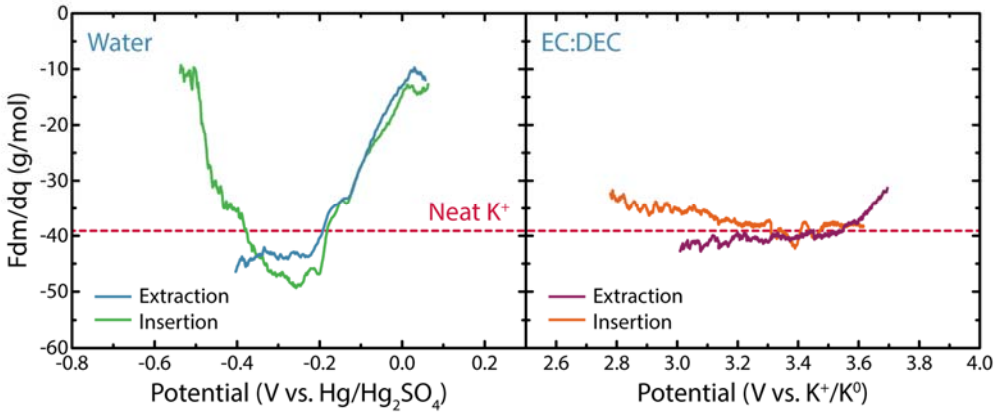

Figure S6. $F\Delta m/\Delta Q$ calculated for a 100 nm thick film (a) in 0.25 mol.L^{-1} K_2SO_4 (pH 3.5) water-based electrolyte during a CV at 10 mV.s^{-1} and (b) in 0.5 mol.L^{-1} KPF_6 EC:DEC-based electrolyte during a CV at 0.5 mV.s^{-1}. The corresponding EQCM data are presented in Figure 2.

8. *Ac*-electrogravimetry[7] theoretical background

When a sinusoidal potential perturbation with low amplitude, ΔE, is imposed to the gold surface/film/electrolyte system (quartz resonator configuration), sinusoidal fluctuations of concentration, ΔC_i, and flux, ΔJ_i, occur such as:

$$\Delta J_i = -d_f \frac{dC_i}{dt} = -j\omega d_f \Delta C_i \qquad \textbf{(Equation S9)}$$

The expression of the global insertion/expulsion flux, ΔJ_i, which depends on the concentration and potential perturbations, at the film/electrolyte interface is:

$$\Delta J_i = \left.\frac{\partial J_i}{\partial C_i}\right|_E \Delta C_i + \left.\frac{\partial J_i}{\partial E}\right|_{C_i} \Delta E = K_i \Delta C_i(d_f) + G_i \Delta E \qquad \textbf{(Equation S10)}$$

where ω is the angular frequency equal to $2\pi f$, f is the perturbation frequency and K_i and G_i are the partial derivatives of the flux, J_i, with respect to the concentration and the potential, $K_i = \left(\frac{\partial J_i}{\partial C_i}\right)_E$ and $G_i = \left(\frac{\partial J_i}{\partial E}\right)_{C_i}$. K_i is the kinetic rate of transfer and G_i is the inverse of the transfer resistance, Rt_i, of the species at the film/electrolyte interface: $Rt_i = \frac{1}{FG_i}$. For each transferred species (i: cation, anion or solvent), the ionic transfer resistance is a good estimation of the ease of the transfer.

Then, the change of the concentration, ΔC_i, of each species with potential ΔE can be calculated using Equation S-9 and Equation S-10, leading to the concentration/potential TF:

$$\frac{\Delta C_i}{\Delta E}(\omega) = \frac{-G_i}{j\omega d_f + K_i} \qquad \textbf{(Equation S11)}$$

Using the concentration/potential TF, the charge/potential transfer function can be calculated, shown for two cationic species, c1 and c2:

$$\begin{aligned} \frac{\Delta q}{\Delta E}(\omega) &= -F d_f \left(\frac{\Delta C_{c1}}{\Delta E}(\omega) + \frac{\Delta C_{c2}}{\Delta E}(\omega)\right) \\ &= -F d_f \left(\frac{-G_{c1}}{j\omega d_f + K_{c1}} + \frac{-G_{c2}}{j\omega d_f + K_{c2}}\right) \end{aligned} \qquad \textbf{(Equation S12)}$$

The Faradaic impedance relative to the global ionic transfer of charged species involved in the charge compensation is:

$$Z_F(\omega) = \frac{\Delta E}{\Delta I_F}(\omega) = \frac{1}{j\omega \frac{\Delta q}{\Delta E}(\omega)} = \frac{1}{j\omega F d_f \left(\frac{G_{c1}}{j\omega d_f + K_{c1}} + \frac{G_{c2}}{j\omega d_f + K_{c2}}\right)} \quad \textbf{(Equation S13)}$$

Finally, the classical electrochemical impedance can be estimated incorporating the electrolyte resistance R_{el} and the interfacial capacitance C_{dl}:

$$\frac{\Delta E}{\Delta I}(\omega) = R_{el} + \frac{1}{j\omega C_{dl} + \frac{1}{Z_F(\omega)}} = R_{el} + \frac{1}{j\omega C_{dl} + j\omega F d_f \left(\frac{G_{c1}}{j\omega d_f + K_{c1}} + \frac{G_{c1}}{j\omega d_f + K_{c2}}\right)} \quad \textbf{(Equation S14)}$$

The second main transfer function can be calculated theoretically taking also into account the charged and uncharged species:

$$\frac{\Delta m}{\Delta E}(\omega) = d_f \left(M_{c1} \frac{\Delta C_{c1}}{\Delta E}(\omega) + M_{c2} \frac{\Delta C_{c2}}{\Delta E}(\omega) + M_s \frac{\Delta C_s}{\Delta E}(\omega) \right) \quad \textbf{(Equation S15)}$$

$$= -d_f \left(M_{c1} \frac{G_{c1}}{j\omega d_f + K_{c1}} + M_{c2} \frac{G_{c2}}{j\omega d_f + K_{c2}} + M_s \frac{G_s}{j\omega d_f + K_s} \right)$$

Partial mass/potential TF can be also estimated by removing one of the cation contribution, calculating for example $\Delta m/\Delta E^{c2,s}(\omega)$.

$$\frac{\Delta m}{\Delta E}^{c2,s}(\omega) = \frac{\Delta m}{\Delta E}(\omega) - \frac{M_{c1}}{F} \frac{\Delta q}{\Delta E}(\omega) \quad \textbf{(Equation S16)}$$

$$\frac{\Delta m^{c2,s}}{\Delta E}(\omega) = d_f\left((M_{c2} - M_{c1})\frac{\Delta C_{c1}}{\Delta E}(\omega) + M_s\frac{\Delta C_s}{\Delta E}(\omega)\right) \quad \textbf{(Equation S17)}$$

This partial TF acts as a cross-check procedure to discriminate between two possible cation couples (K^+/H^+ and K^+/H_3O^+). A partial mass/potential TF can be also estimated for the other cation $\Delta m/\Delta E^{c1,s}(\omega)$ but not in the case of a solvent molecule.

The derivative of the concentration for each species with respect to the potential can be calculated by considering the low frequency limit of $\Delta C_i/\Delta E(\omega)$.

$$\frac{\Delta C_i}{\Delta E}(\omega) = \frac{-G_i}{j\omega d_f + K_i} \xrightarrow[\omega\to 0]{} -\frac{G_i}{K_i} \quad \textbf{(Equation S18)}$$

Then, ΔC_i is obtained by integrating $-\frac{G_i}{K_i}$ with respect to the potential. To finish, Δm_i is acquired by multiplying ΔC_i by the volume of active material. The global mass variation at each potential can therefore be calculated with the sum of each Δm_i in order to be compared with the classical EQCM measurement, as a cross-check calculation to verify the fitting procedure and the adequacy of the selected model.

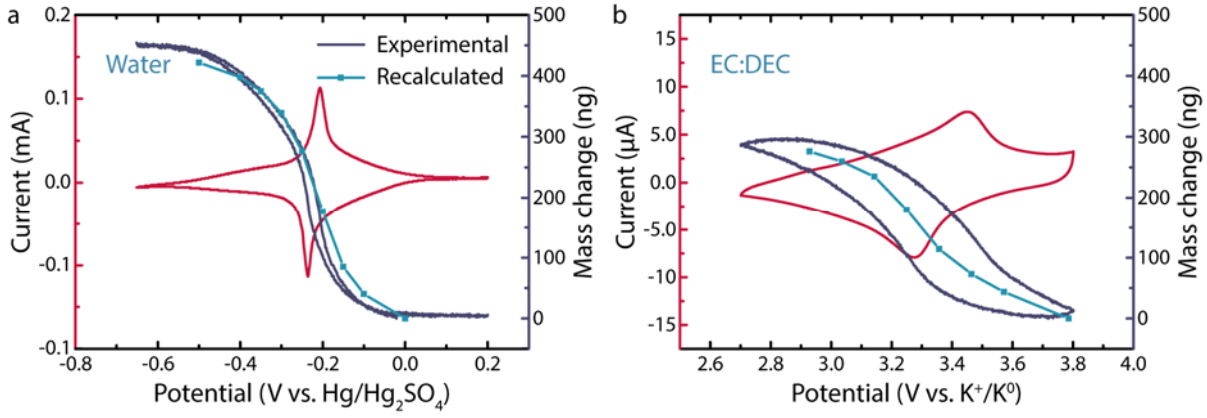

Figure S7. Comparison of the mass variation by classical EQCM measurement at 5 mV.s^{-1} with recalculated mass variation by *ac*-electrogravimetry in (a) water and (b) ED:DEC-based electrolytes.

9. Typical snapshots of the Classical Molecular Dynamics simulations of 0.25 mol.L^{-1} K_2SO_4 in H_2O and 0.5 mol.L^{-1} KPF_6 in EC:DEC (50:50) at interfaces with a gold electrode

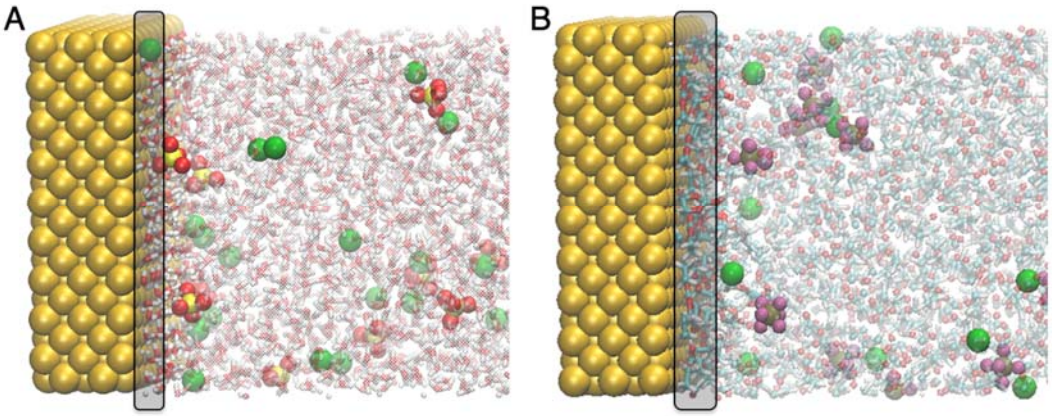

Figure S8. Representative snapshots extracted from the MD simulations of K_2SO_4 in H_2O (A) and KPF_6 in EC/DEC (B). Au atoms are represented in dark yellow, K^+ cations in green, and SO_4^{2-} and PF_6^- anions in yellow/red and brown/violet, respectively. Solvent molecules belonging to the first layer in contact with the Au surface are highlighted.

10. Classical Molecular Dynamics simulations of 1M $LiClO_4$ in H_2O and PC

Classical MD simulations of 1 mol.L^{-1} $LiClO_4$ in H_2O and 1 mol.L^{-1} $LiClO_4$ in propylene carbonate (PC) between two planar Au(100) electrodes at a fixed potential difference of 0 V were performed with the MetalWalls code.[8] Each electrode is made of 5 layers, 162 Au atoms each, while the electrolyte is composed of 100 $LiClO_4$ ion pairs and 5500 H_2O molecules for the aqueous system and of 100 $LiClO_4$ ion pairs and 1170 PC molecules for the non-aqueous system. The SPC/E[9] model was chosen for water, while force field parameters for PC were taken from OPLS[10] with charges adopted in Chaudhari *et al.*[11] The Lennard-Jones parameters for Li^+ were taken from OPLS,[9] while force field parameters for ClO_4^- from Ref [12]. Finally, Lennard-Jones parameters introduced by Heinz *et al.*[13] were adopted for Au(100). Mixed Lennard–Jones parameters for all of the different atom types were obtained using the Lorentz–Berthelot combination rules.

2D periodic boundary conditions were employed, with no periodicity on the direction normal to the Au surface and box dimensions along x and y directions of Lx = Ly = 36.63 Å.

Electrostatic interactions were computed using a 2D Ewald summation method, with a cut-off of 12 Å for the short-range part. The simulation boxes were equilibrated at constant atmospheric pressure by applying a constant pressure force to the electrodes. The electrodes separation was then fixed to the equilibrium value. An equilibration run of 2 ns in the NVT ensemble (T = 298K) was then performed. After equilibration, production runs of 30 ns and 40 ns for $LiClO_4$ in H_2O and $LiClO_4$ in PC, respectively, have been collected in the NVT ensemble (T = 298K), with the electrodes potential fixed to 0 V, and using a timestep of 1 fs.

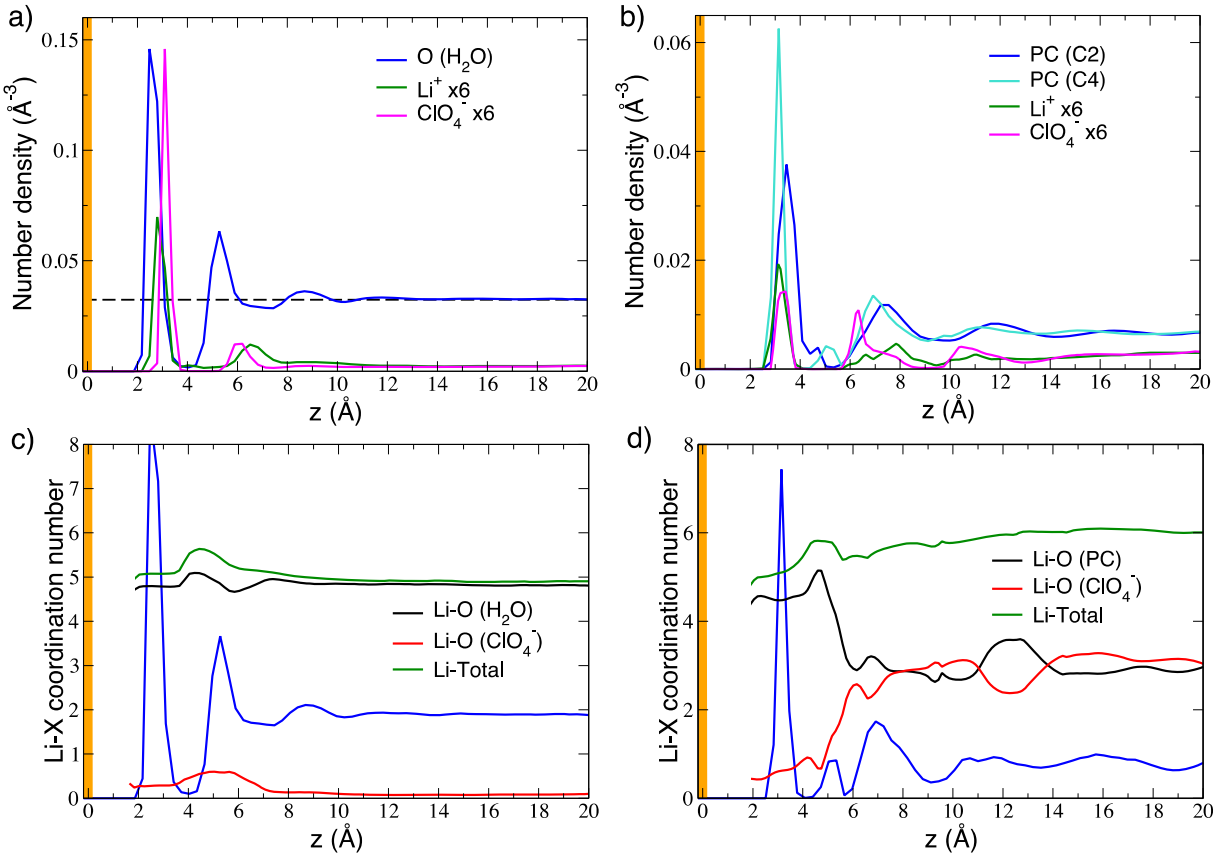

Figure S9. (a,b) Density profiles for ions and solvent molecules in the direction normal to the surface (z) for (a) 1 mol.L^{-1} $LiClO_4$ in H_2O and (b) 1 mol.L^{-1} $LiClO_4$ in PC. C2 refers to the carbon atom of the ring linked to the methyl group, while C4 is the carbon atom of the carbonyl group. Density profiles of the ions were multiplied because of their much lower concentrations with respect to the solvents. (c,d) Evolution of the Li-solvent, Li-anion and Li-Total (solvent + anion) coordination number as a function of the distance z from the surface (c) in water and (d) in PC. In the aqueous system, the O atom of H_2O and ClO_4^- have been considered. In the organic system, the carbonyl group oxygen atom of PC is used to define the coordination number of the solvent, while the O atoms are considered for the anions. The density profiles of water and PC, and surface atoms are also plotted in panels (c) and (d). For all coordination numbers, the cut-off values correspond to the first minimum of the respective radial distribution functions.

References

1. Montella, C., Discussion of the potential step method for the determination of the diffusion coefficients of guest species in host materials: Part I. Influence of charge transfer kinetics and ohmic potential drop. *J. Electroanal. Chem.* **2002,** *518* (2), 61-83.
2. Kim, Y.-S.; Kriegel, S.; Harris, K. D.; Costentin, C.; Limoges, B.; Balland, V., Evidencing Fast, Massive, and Reversible H+ Insertion in Nanostructured TiO2 Electrodes at Neutral pH. Where Do Protons Come From? *The Journal of Physical Chemistry C* **2017,** *121* (19), 10325-10335.
3. Johannsmann, D., The Quartz Crystal Microbalance in Soft Matter Research: Fundamentals and Modeling; Soft and Biological Matter. *Springer International Publishing* **2015**.
4. Sauerbrey, G., Verwendung von Schwingquarzen zur Wägung dünner Schichten und zur Mikrowägung. *Zeitschrift für Physik* **1959,** *155* (2), 206-222.
5. Buser, H. J.; Schwarzenbach, D.; Petter, W.; Ludi, A., The crystal structure of Prussian Blue: Fe4[Fe(CN)6]3.xH2O. *Inorg. Chem.* **1977,** *16* (11), 2704-2710.
6. Herren, F.; Fischer, P.; Ludi, A.; Haelg, W., Neutron diffraction study of Prussian Blue, Fe4[Fe(CN)6]3.xH2O. Location of water molecules and long-range magnetic order. *Inorg. Chem.* **1980,** *19* (4), 956-959.
7. Gabrielli, C.; García-Jareño, J. J.; Keddam, M.; Perrot, H.; Vicente, F., Ac-Electrogravimetry Study of Electroactive Thin Films. I. Application to Prussian Blue. *The Journal of Physical Chemistry B* **2002,** *106* (12), 3182-3191.
8. Marin-Laflèche, A. H., M.; Scalfi, L.; Coretti, A.; Dufils, T.; Jeanmairet, G.; Reed, S. K.; Serva, A.; Berthin, R.; Bacon, C.; Bonella, S.; Rotenberg, B.; Madden, P. A.; Salanne, M., MetalWalls: A classical molecular dynamics software dedicated to the simulation of electrochemical systems. *Journal of Open Source Software* **2020,** *5* (53), 2373-2378.
9. Berendsen, H. J. C.; Grigera, J. R.; Straatsma, T. P., The missing term in effective pair potentials. *The Journal of Physical Chemistry* **1987,** *91* (24), 6269-6271.
10. Jorgensen, W. L.; Maxwell, D. S.; Tirado-Rives, J., Development and Testing of the OPLS All-Atom Force Field on Conformational Energetics and Properties of Organic Liquids. *J. Am. Chem. Soc.* **1996,** *118* (45), 11225-11236.
11. Chaudhari, M. I.; Nair, J. R.; Pratt, L. R.; Soto, F. A.; Balbuena, P. B.; Rempe, S. B., Scaling Atomic Partial Charges of Carbonate Solvents for Lithium Ion Solvation and Diffusion. *Journal of Chemical Theory and Computation* **2016,** *12* (12), 5709-5718.
12. Liu, X.; Zhang, S.; Zhou, G.; Wu, G.; Yuan, X.; Yao, X., New Force Field for Molecular Simulation of Guanidinium-Based Ionic Liquids. *The Journal of Physical Chemistry B* **2006,** *110* (24), 12062-12071.
13. Heinz, H.; Vaia, R. A.; Farmer, B. L.; Naik, R. R., Accurate Simulation of Surfaces and Interfaces of Face-Centered Cubic Metals Using 12−6 and 9−6 Lennard-Jones Potentials. *The Journal of Physical Chemistry C* **2008,** *112* (44), 17281-17290.